

This is the accepted manuscript made available via CHORUS. The article has been published as:

Relativistic simulations of eccentric binary neutron star mergers: One-arm spiral instability and effects of neutron star spin

William E. East, Vasileios Paschalidis, Frans Pretorius, and Stuart L. Shapiro

Phys. Rev. D **93**, 024011 — Published 8 January 2016

DOI: [10.1103/PhysRevD.93.024011](https://doi.org/10.1103/PhysRevD.93.024011)

Relativistic Simulations of Eccentric Binary Neutron Star Mergers: One-arm Spiral Instability and Effects of Neutron Star Spin

William E. East¹, Vasileios Paschalidis², Frans Pretorius²

¹*Kavli Institute for Particle Astrophysics and Cosmology, Stanford University,
SLAC National Accelerator Laboratory, Menlo Park, CA 94025, USA*

²*Department of Physics, Princeton University, Princeton, NJ 08544, USA*

and

Stuart L. Shapiro^{3,4}

³*Department of Physics, University of Illinois at Urbana-Champaign, Urbana, IL 61801*

⁴*Department of Astronomy & NCSA, University of Illinois at Urbana-Champaign, Urbana, IL 61801*

We perform general-relativistic hydrodynamical simulations of dynamical capture binary neutron star mergers, emphasizing the role played by the neutron star spin. Dynamical capture mergers may take place in globular clusters, as well as other dense stellar systems, where most neutron stars have large spins. We find significant variability in the merger outcome as a function of initial neutron star spin. For cases where the spin is aligned with the orbital angular momentum, the additional centrifugal support in the remnant hypermassive neutron star can prevent the prompt collapse to a black hole, while for antialigned cases the decreased total angular momentum can facilitate the collapse to a black hole. We show that even moderate spins can significantly increase the amount of ejected material, including the amount unbound with velocities greater than half the speed of light, leading to brighter electromagnetic signatures associated with kilonovae and interaction of the ejecta with the interstellar medium. Furthermore, we find that the initial neutron star spin can strongly affect the already rich phenomenology in the post-merger gravitational wave signatures that arise from the oscillation modes of the hypermassive neutron star. In several of our simulations, the resulting hypermassive neutron star develops the one-arm ($m = 1$) spiral instability, the most pronounced cases being those with small but non-negligible neutron star spins. For long-lived hypermassive neutron stars, the presence of this instability leads to improved prospects for detecting these events through gravitational waves, and thus may give information about the neutron star equation of state.

PACS numbers: 04.25.D-, 04.25.dk, 04.30.-w

I. INTRODUCTION

The challenge of understanding the inspiral and merger of compact binaries, such as neutron star–neutron star (NSNS) and black hole–neutron star (BHNS) binaries, has attracted considerable attention in recent years. These systems are potential probes of fundamental physics, from strong-field gravity to the super nuclear density physics which determines the NS equation of state (EOS). They are also “multimessenger” sources in the sense that they are among the primary targets of gravitational wave (GW) observations by ground-based laser interferometers such as aLIGO [1], VIRGO [2], and KAGRA [3], as well as potentially giving rise to a number of electromagnetic (EM) transients, either before [4–10] or after [11–14] the merger event itself. The EM transients accompanying GW events are possible sources for current or upcoming telescopes, e.g. PTF [15], PanSTARRS [16], or LSST [17]. Moreover, compact binary mergers could be integral to solving several outstanding astrophysical puzzles, such as determining the progenitors of short-hard gamma ray bursts (see e.g. [18–20]) and the origin of r-process elements in the Universe [21].

In this paper we focus on eccentric binary neutron star mergers. Accurately modeling such strong-field events,

where spacetime is both strongly curved and very dynamic, requires the use of full general relativity (GR). Studies of NSNS binaries with numerical relativity have largely focused on quasicircular inspiral and mergers, see, e.g., [22, 23] for reviews, and [24–32] and references therein for more recent work. The predominant channel thought to lead to quasicircular NSNS mergers is the evolution of isolated stellar binary systems, so-called primordial binaries. Here, given the typical separation at which a binary NS system is born (after both massive stars have collapsed to neutron stars), gravitational radiation will drive the orbit to very close to circular well before emission reaches frequencies observable by ground-based detectors (which for simplicity we call the “LIGO band”). Recent analysis [33–37], however, suggests that in addition to these so-called field binaries, there may be a population of compact binaries that are assembled in globular clusters (GCs), galactic nuclei, and other dense stellar systems via dynamical capture or exchange interactions. Some fraction of these systems will emit GWs in the LIGO band while the orbit is still highly eccentric (for leading-order estimates of these fractions and related timescales see the discussions in [36, 38]). While such events will occur less frequently than quasicircular inspirals (whether from field binaries or dynamically assembled), they will have a distinct phenomenology and

observational signature, including a repeated-burst phase of the GW signal, and possibly distinguishable EM transients (e.g. [10]).

While there is considerable uncertainty about the rates of eccentric NSNS mergers, there have been estimates of up to $\sim 50 \text{ yr}^{-1} \text{ Gpc}^{-3}$ (see e.g., [35, 39, 40] and discussions therein). Although it is unknown whether high eccentricity NSNS mergers take place with enough frequency to be relevant for LIGO, or whether their observation with GWs may require third-generation GW interferometers such as the Einstein Telescope [41], it is plausible that they do occur at rates relevant for EM observations. For example, the spatial offset of some short gamma-ray bursts (sGRBs) from their host galaxies is inconsistent with merging NSNS that reside in the galactic disks [42]. Using simulations to scale from the NSNS binary observed in the GC M15 in our Galaxy, it is argued in [42] that NSNS mergers in GCs may be responsible for $\sim 10 - 30\%$ of the observed sGRBs (see also [43–45]). On the order of a percent of NSNS mergers resulting from binary-single exchange interactions in GCs are likely to take place at moderate to high eccentricities [36], while essentially all dynamical capture mergers will have a high eccentricity phase within the LIGO band, though the latter class of event is expected to occur much less frequently. Also, rate estimates are not known for less well understood mechanisms for creating eccentric binaries, like resonances in triple systems [46–48], though a recent study [49] finds that aLIGO detection rates for black hole mergers induced by the Lidov-Kozai mechanism can be 2 yr^{-1} , with about 20% of these entering the aLIGO band with finite eccentricity. However, they report that this process makes negligible contribution to NSNS mergers.

Fully general-relativistic hydrodynamical (GR-HD) simulations of dynamical-capture NSNS mergers with nonspinning NSs were performed in [39, 40] (see also [50, 51] for work on BHNS eccentric mergers with nonspinning NSs, and [52, 53] for eccentric NSNS mergers within Newtonian gravity). These studies revealed several interesting properties of such events, including the distinctive character of the GW signals, the excitation of f-mode oscillations during close encounters, the dependency on whether or not a BH forms immediately upon merger on the initial impact parameter of the encounter (in addition to the dependence on the NS EOS, a fact well known from studies of quasi-circular mergers), and the fact that the impact parameter and EOS can significantly affect the properties of the BH accretion disk (in the case of prompt BH formation) and ejected material.

However, as pointed out in [54], mergers stemming from dynamically assembled NS binaries in GCs likely involve rapidly spinning NSs, simply because the NSs residing in GCs are primarily found to be millisecond pulsars (MSPs), and MSPs have very long inferred spin-down timescales. We briefly recall the arguments presented in that reference here. Approximately 83% of all the observed pulsars in GCs are MSPs [55],

the fastest spinning of which has a spin period P_s of $\sim 1.4 \text{ ms}$. This is connected to the fact that GCs are ideal environments for forming low-mass X-ray binaries (LMXB) [56] where mass and angular momentum can be transferred to the NS from its companion, spinning the star up to a period of milliseconds. This process, referred to as pulsar “recycling,” typically occurs on the pulsar spin-relaxation time $t_{\text{spin}} \sim 10^7 (P_s/2.5\text{ms})^{-1} (\dot{M}/0.1\dot{M}_E)^{-0.87} \text{ yr}$ (see e.g. [57]), where \dot{M} is the accretion rate and \dot{M}_E the Eddington accretion rate. Thus, after a LMXB forms, NS spin-up occurs very rapidly until the so-called spin-equilibrium value $P_{s,\text{eq}} \simeq 2.0 B_8^{6/7} (\dot{M}/0.1\dot{M}_E)^{-3/7} R_{\text{NS},15}^{18/7} \text{ ms}$ [58, 59], where B_8 is the NS polar magnetic field in units of 10^8 G and $R_{\text{NS},15}$ the NS radius in units of 15 km . In the above estimates, a canonical NS mass of $M_{\text{NS}} = 1.4 M_\odot$ is assumed.

MSPs tend to have low inferred polar magnetic field strengths ($3 \times 10^7 - 3 \times 10^8 \text{ G}$ [57]), and hence have very long magnetic dipole spin-down timescales $t_{\text{sd}} \sim 3.0 I_{45} B_8^{-2} P_{s,2.5}^2 R_{\text{NS},15}^{-6} \text{ Gyr}$ [54], where I_{45} is the NS moment of inertia in units of 10^{45} g cm^2 and $P_{s,2.5}$ the spin period in units of 2.5 ms . Since the estimates in [35] suggest a rate of NSNS collisions occurring in GCs of $\sim 10 \text{ Gyr}^{-1}$ per Milky Way-equivalent galaxy, the long amount of time required for spin down makes it seem likely that a portion of such mergers will involve MSPs.

To date, only one confirmed NSNS system in a GC is known: the PSR B2127+11C in M15, which is a 30 ms pulsar with eccentricity $e \simeq 0.68$ [60]. There is also a candidate NSNS system PSR J1807-2500B in the GC NGC 6544 with a 4.19 ms pulsar, eccentricity $e \simeq 0.75$, and the most massive companion ($> 1.2 M_\odot$) known orbiting a fully recycled pulsar. Here it is unlikely that the progenitor of the companion could have recycled the pulsar [61], thus giving some observational evidence that dynamically assembled NSNS binaries with highly spinning NSs can indeed form in GCs. A more detailed estimate of expected distribution of spins for binary NSs at the time of merger would necessitate a dynamical encounter calculation along the lines of [36], but also keeping track of the changing NS spins and magnetic field strengths.

For spinning NSs with periods on the order of milliseconds, spin strongly affects the NS structure — among other things, making the star less compact and providing additional centrifugal support against collapse — and in binaries it can change the orbital dynamics [54, 62]. Thus, realistic modeling of eccentric NSNS mergers as they may arise in GCs should treat NS spin. To date, the only simulations in full GR accounting for the NS spin self-consistently have focused either on quasicircular NSNS mergers, e.g. [27, 62–65] (see also [66, 67]), or eccentric BHNS mergers [54]. These studies showed the importance even moderate NS spins can have on determining the dynamics of the merger and its outcome. On the other hand, recent work in [68] adopting the conformal flatness approximation to GR simulated quasicircu-

lar NSNS mergers to study the effects of NS spin aligned with orbital angular momentum on the post-merger oscillation frequencies of hypermassive NSs (HMNSs) found that unless the NS spin is very high, the oscillation frequencies are practically unaffected. However, spin increases the uncertainty of inferring the NS EOS from these oscillation modes.

Here we perform a companion study to [54] with the goal of understanding the role of spin in eccentric NSNS mergers. We show that spin can have a number of important effects including: significantly affecting the amount and velocity distribution of the unbound material produced post-merger; modifying the qualitative structure of the GW signal; and determining whether a merger will produce a long-lived, but transient, HMNS versus promptly collapsing to a BH (which also affects the two aforementioned characteristics). A remarkable feature discovered in a number of our simulations (and first reported in [69]) is that the HMNSs formed after merger develop the so-called one-arm ($m = 1$) spiral instability.

The one-arm instability in rotating stars was first discovered using hydrodynamic simulations of Newtonian polytropes with soft equations of state and a high degree of differential rotation [70]. Guided by Newtonian hydrodynamic simulations, in [71] it was suggested that a toroidal density configuration is necessary to trigger the instability, and based on observations reported in [72], [73] argued that like the low- $T/|W|$ dynamical (bar-mode) instability [74, 75], the one-arm spiral instability develops near the corotation radius, i.e., the locus where the angular frequency of the unstable mode coincides with a local rotational angular velocity of the fluid. This expectation seems to be confirmed both by Newtonian [76] and general-relativistic [77] simulations of isolated differentially rotating stars. In [76] it was further shown that the one-arm spiral instability can develop even for stiff EOSs ($\Gamma = 2$), as well as for non-toroidal configurations, as long as the radial vortensity profile exhibits a local minimum. In [78], $m = 1$ modes were triggered in general-relativistic magnetohydrodynamic simulations of the low- $T/|W|$ instability of isolated stars. In addition, the instability has been found to occur in the neutron star cores formed in hydrodynamic core-collapse simulations [79–81]. Although growing $m = 1$ modes in the equatorial plane of HMNS remnants of quasicircular NSNS mergers with spinning neutron stars were reported in [63], they were explained to arise due to mode couplings. Here we expand upon the results presented in [69] by probing the instability with a more complete parameter survey and performing a resolution study. While we find growing $m = 1$ density modes in many cases following merger, the one-arm spiral instability is fully developed (the $m = 1$ azimuthal density mode dominates over all other modes) by the termination of our simulations only for cases where the total angular momentum (spin plus orbital) remaining at merger $J/M^2 \sim 0.9$ – 1.0 . This part of the parameter space is also of interest for quasicircular mergers. The characteristic growth time of the

instability is on the order of milliseconds and saturates ~ 10 ms following merger. We demonstrate that the instability is imprinted on the GWs from the post-merger phase. In particular, the GW signal is quasi-periodic, with the GW fundamental frequencies being commensurate with the dominant frequencies of azimuthal density modes. If the one-arm instability persists in HMNS remnants that live on the order of a second, the GWs could be detectable by aLIGO at ~ 10 Mpc and by the Einstein Telescope ~ 100 Mpc. We speculate as to how the instability may help to constrain the EOS of the matter above nuclear saturation.

The remainder of the paper is structured as follows. In Sec. II we describe the parameters we consider and our numerical methods for constructing initial data and evolving spinning binary NSs. In Sec. III we present our simulation results, including detailing the dynamics, properties of post-merger remnants, GW signals, potential EM counterparts, as well as a comprehensive analysis of the development of the one-arm spiral instability, and how NS spin affects all of the above. We conclude in Sec. IV. Geometrized units where $G = c = 1$ are used throughout, unless otherwise specified. Greek indices run from 0 to 3 and Latin indices from 1 to 3.

II. NUMERICAL APPROACH

We use the code described in [82] to evolve the GR-HD equations and simulate NSNS mergers with spinning NSs. We solve the Einstein field equations in the generalized-harmonic formulation with fourth-order accurate finite differences. The hydrodynamic equations are evolved in conservative form using high-resolution shock-capturing techniques as specified in [51].

A. Initial conditions

We construct initial data for our evolutions that satisfies the constraint equations as explained in [69, 83]. We begin by constructing equilibrium solutions for isolated rigidly-rotating NSs with the code described in [84, 85]. We then determine the free-data for the metric and matter fields by superposing two such boosted NS solutions, with the velocities and positions of a marginally unbound Newtonian orbit at a separation of $d = 50M$ (~ 200 km; where M is the total ADM mass), and solve the constraints. At this initial separation, the NSs maintain their equilibrium profiles with only small-amplitude perturbations excited such that the maximum density oscillates with $\delta\rho_{\max}/\rho_{\max} \lesssim 5\%$. The NS EOS we use is the piece-wise polytrope labelled “HB” in [86], which yields a maximum mass for nonspinning neutron stars of $2.12M_{\odot}$ —the Tolman-Oppenheimer-Volkov (TOV) limit. Using the code of [84, 85] we find that when allowing for maximal uniform rotation the maximum mass (also known as the “supramassive” limit) for the HB

TABLE I. Properties of isolated NS models considered in this work. Listed are the dimensionless NS spin a_{NS} , spin period P_s in ms, rest-mass M_0 in M_\odot , circumferential equatorial radius R_{NS} in km, compaction $C = M_{\text{NS}}/R_{\text{NS}}$, and ratio of kinetic T to potential $|W|$ energy. All models have a gravitational mass of $M = 1.35 M_\odot$.

a_{NS}	$P_s(\text{ms})$	$M_0(M_\odot)$	$R_{\text{NS}}(\text{km})$	C	$\frac{T}{ W } \times 100$
0.756	0.99	1.46	16.52	0.12	12.09
0.400	1.45	1.48	12.42	0.16	3.91
0.200	2.68	1.49	11.78	0.17	1.02
0.100	5.25	1.49	11.63	0.17	0.26
0.075	7.02	1.49	11.61	0.17	0.14
0.050	10.62	1.49	11.60	0.17	0.06
0.025	20.94	1.49	11.59	0.17	0.02
0.000	∞	1.49	11.58	0.17	0.00

EOS is $2.53M_\odot$, which is $\sim 19\%$ larger than the TOV limit – a result anticipated from the analysis presented in [87]. To account for the possibility of heating due to shocks, we also add a thermal component to the pressure: $P_{\text{th}} = 0.5\epsilon_{\text{th}}\rho_0$ where ϵ_{th} is the thermal part of the internal specific energy and ρ_0 is the rest mass density.

We fix the gravitational (ADM) mass of each NS to $M_{\text{NS}} = 1.35 M_\odot$, and consider NSs with dimensionless spins $a_{\text{NS}} = J_{\text{NS}}/M_{\text{NS}}^2 = 0, 0.025, 0.05, 0.075, 0.1, 0.2, 0.3, 0.4$, and 0.75 . As a result, the total ADM mass of the binaries we construct is $\sim 6\%$ larger than the supramassive limit mass. In Table I we list several properties of the NS models we consider in this work. The spin periods of the rotating models cover the range of observed GC MSPs. The ratio of kinetic to gravitational potential energy $T/|W|$ for our spinning NS models is ≤ 0.12 , and thus all of these models are stable against the development of the dynamical bar mode instability [88, 89]. The most rapidly spinning NS considered here has ratio of polar to equatorial radius of $r_{po}/r_{eq} = 0.55$, slightly above the mass-shedding limit of this EOS of $r_{po}/r_{eq} = 0.543$. For the simulations considered here, we restrict ourselves to cases where the NS spin is either aligned or anti-aligned with the orbital angular momentum of the system (the latter indicated by a negative value of a_{NS}).

In addition to the NS spin, we also vary the initial impact parameter of the binary. We label this parameter by the periastron distance r_p of the corresponding marginally unbound Newtonian orbit (which will differ from the actual periastron of the binary, some of which, for example, merge on the first encounter). Here we consider cases with $r_p/M \in [5, 10]$ (see Table II for a list of all cases excluding those with $r_p/M = 10$, which were not followed through merger). For computational expediency, we focus on cases with smaller periastron values, since cases with larger periastron values will undergo a series of close encounters with lengthy elliptic orbits in between before finally merging.

B. Diagnostics

In the analysis below, and in particular for studying the evolution of the hypermassive NS that forms post-merger in some cases, we will make use of several quantities which we define here. One is the complex azimuthal mode decomposition of the conserved rest-mass density as a function of cylindrical coordinate radius ($\varpi = \sqrt{x^2 + y^2}$) and z

$$C_m(\varpi, z) = \frac{1}{2\pi} \int_0^{2\pi} \rho_0 u^0 \sqrt{-g} e^{im\phi} d\phi, \quad (1)$$

where ϕ is the azimuthal angle in cylindrical coordinates, and this quantity integrated throughout the star

$$C_m = \int \rho_0 u^0 \sqrt{-g} e^{im\phi} d^3x, \quad (2)$$

where u^μ is the fluid 4-velocity, and g the determinant of the spacetime metric. We also track the xy-component of the vorticity 2-form

$$\Omega_{\mu\nu} = \nabla_\mu(hu_\nu) - \nabla_\nu(hu_\mu) \quad (3)$$

on the equatorial plane. Here ∇_μ is the covariant derivative and $h = 1 + \epsilon + P/\rho_0$ is the specific enthalpy, where ϵ is the internal specific energy and P the pressure. In addition to the above, we compute the ratio of total kinetic (T_{kin}) or rotational kinetic (T_{rot}) energy to the gravitational potential energy $|W|$, where [90]

$$T_{\text{kin}} = \frac{1}{2} \int T^0{}_i v^i \sqrt{-g} d^3x, \quad (4)$$

$$v^i = u^i/u^0,$$

$$T_{\text{rot}} = \frac{1}{2} \int T^0{}_\phi v^\phi \sqrt{-g} d^3x, \quad (5)$$

and

$$W = M_0 + E_{\text{int}} + T_{\text{kin}} - M_{\text{ADM}}. \quad (6)$$

M_0 is the rest-mass and E_{int} is the internal energy

$$E_{\text{int}} = \int \rho_0 u^0 \epsilon \sqrt{-g} d^3x. \quad (7)$$

In Eqs. (4) and (5), $T^\mu{}_\nu$ is the stress-energy tensor of the perfect fluid. Equations (1), (2) and (5) are computed in a coordinate center-of-mass frame of the HMNS whose spatial coordinates are

$$x_{\text{cm}}^i = \frac{1}{M_0} \int x^i \rho_0 u^t \sqrt{-g} d^3x. \quad (8)$$

We caution that the above diagnostics are not gauge-independent, and Eqs. (4)-(7) are strictly applicable only in stationary and axisymmetric spacetimes, where Eqs. (5)-(7) can be shown to be gauge invariant (see e.g. [23] p. 464 and [84, 85]). However, they are helpful in illustrating various features of the instability and comparing them to previous studies. In addition, following merger the HMNS reaches a quasi-steady state, and the spacetime is not too far from being axisymmetric.

TABLE II. Summary of simulations followed through merger

$\frac{r_p}{M}$	$a_{\text{NS},1}$	$a_{\text{NS},2}$	$\frac{J_{\text{ADM}}}{M^2}$	$\frac{E_{\text{GW}} \times 100}{M}$	$\frac{J_{\text{GW}} \times 100}{M^2}$	$\langle \epsilon_{\text{th}} \rangle$	$\frac{E_{\text{th}}}{E_{\text{int}}}$	$M_{0,u}$	$\langle v_{\infty} \rangle$	$E_{\text{kin},51}$	L_{41}	t_{peak}	F_{ν}	t_F	τ_{min}
5.0	0.00	0.00	0.77	1.03	6.66	11		0.02	0.42	0.05	0.36	0.04	0.08	1.3	BH
5.0	-0.20	0.20	0.77	1.01	6.59	14		0.03	0.43	0.09	0.43	0.05	0.14	1.5	BH
5.0	0.05	0.05	0.79	1.12	7.12	10		0.02	0.40	0.05	0.35	0.04	0.07	1.4	BH
5.0	0.00	0.20	0.82	1.22	7.61	12		0.05	0.42	0.11	0.52	0.06	0.16	1.7	BH
5.0	0.10	0.10	0.82	1.23	7.69	22		0.03	0.35	0.06	0.40	0.05	0.05	1.8	BH
5.0	0.00	0.40	0.87	2.25	16.6	24	0.29	4.14	0.24	3.87	3.66	0.46	1.29	13.5	24
5.0	0.20	0.20	0.87	3.40	24.5	21	0.23	4.74	0.23	3.52	3.81	0.48	1.01	14.3	22
5.0	0.40	0.40	0.97	1.40	11.4	25	0.33	2.83	0.19	1.28	2.64	0.33	0.20	14.6	11
6.0	0.00	0.00	0.84	3.14	23.1	28	0.27	3.51	0.26	3.29	3.48	0.43	1.30	11.5	8
6.0	0.00	0.40	0.94	1.58	13.1	23	0.31	1.28	0.24	0.99	2.00	0.25	0.31	8.9	24
6.0	0.40	0.40	1.04	0.94	8.92	21	0.33	0.37	0.13	0.10	0.78	0.10	0.01	11.7	23
8.0	-0.40	-0.40	0.78	2.37	15.4	6		0.26	0.37	0.48	1.13	0.14	0.51	3.3	BH
8.0	0.00	0.00	0.98	2.11	17.8	23	0.28	0.35	0.20	0.20	0.98	0.12	0.04	6.6	26
8.0	-0.40	0.40	0.98	0.83	9.07	38	0.42	4.11	0.17	1.59	3.08	0.39	0.21	17.4	8
8.0	-0.10	0.10	0.97	1.58	14.8	22	0.29	0.29	0.22	0.19	0.92	0.12	0.05	5.6	9
8.0	0.025	0.05	0.99	1.68	16.0	20	0.28	0.65	0.19	0.29	1.28	0.16	0.05	8.6	32
8.0	0.05	0.05	1.00	1.51	15.0	20	0.28	0.78	0.19	0.33	1.39	0.17	0.05	9.2	27
8.0	0.05	0.075	1.00	1.36	14.0	18	0.28	0.84	0.19	0.36	1.46	0.18	0.06	9.3	32
8.0	0.10	0.10	1.02	1.58	15.6	18	0.25	1.13	0.18	0.46	1.66	0.21	0.07	10.5	40
8.0	0.00	0.40	1.075 ⁿ	1.01	11.0	23	0.32	5.96 ^o	0.182 ^p	2.26 ^q	3.80	0.48	0.34	18.1	23
8.0	0.20	0.20	1.07	1.37	14.7	15	0.27	3.39	0.17	1.10	2.78	0.35	0.14	15.9	12
8.0	0.40	0.40	1.17	0.82	10.9	13	0.24	8.07	0.18	3.01	4.44	0.56	0.47	19.7	20
8.0	0.75	0.75	1.35	0.46	8.33	12	0.27	16.73	0.22	9.00	7.00	0.87	2.29	21.0	16
9.0	0.40	0.40	1.24	2.58	41.0	7	0.12	6.28	0.12	1.06	3.22	0.40	0.06	26.8	16

For $r_p/M \geq 10.0$ only the first fly-by encounter was modeled and these cases are not listed.

^a J_{ADM} = global angular momentum, M = total ADM mass

^b Total energy emitted in GWs through the $r = 100M$ surface. For HMNS cases, we only include the first 8 ms after merger.

^c Total angular momentum emitted in GWs. For HMNS cases, we only include the first 8 ms after merger.

^d Rest-mass density weighted average of the thermal specific energy in units of MeV per neutron mass.

^e Ratio of thermal (Eulerian) internal energy to total internal energy measured ≈ 7 ms after merger.

^f Unbound rest mass in percent of M_{\odot} .

^g Rest-mass averaged asymptotic velocity of unbound material.

^h Kinetic energy of ejecta in units of 10^{51} erg.

ⁱ Kilonovae bolometric luminosity in units of 10^{41} erg s $^{-1}$ using Eq. (10).

^j Kilonovae luminosity rise time in units of days using Eq. (9).

^k Specific brightness of radio waves from interaction of ejecta with the ISM in units of mJy using Eq. (12). for $n_0 = 0.1$ cm $^{-3}$, $\nu = 1$ GHz, $d = 100$ Mpc.

^l Rise time of Ejecta-ISM signal in units of years using Eq. (11).

^m Lower limit on the HMNS lifetime in ms set by the simulated time and measured from the time the stars make contact immediately before merger. BH implies that a BH formed promptly after merger.

ⁿ Richardson extrapolated value using all three resolutions is 1.071.

^o Richardson extrapolated value using all three resolutions is 5.88.

^p Richardson extrapolated value using all three resolutions is 0.177.

^q Richardson extrapolated value using all three resolutions is 2.19.

C. Resolution

In the simulations described here we used adaptive mesh refinement (AMR), and include flux corrections to avoid breaking the conservative nature of the hydrodynamic evolution at AMR boundaries [82]. The AMR hierarchy contains six levels that are periodically adjusted during the evolution based on estimates of the metric

truncation error. Most simulations were performed using a base-level resolution with 201^3 points, and finest-level resolution with approximately 100 points covering the (nonspinning) NS diameter. For several cases ($r_p/M = 8$, $a_{\text{NS},1} = 0$, $a_{\text{NS},2} = 0.4$, and spin parameters in Sec. III D of relevance to the one-arm instability) we also ran simulations at 0.64 and $1.28\times$ the resolution, to establish convergence and estimate truncation error. Results from

one such resolution study are shown in Fig. 1. There we demonstrate that the constraint part of the field equations are converging at the expected order (second order before merger and at latter times, and first order during the merger when shocks form), and indicate the gravitational wave signal and amount of unbound material as a function of asymptotic velocity, measured for this case at the three different resolutions. More convergence results are presented later in Sec.III D.

III. RESULTS AND DISCUSSION

We simulate a number of binary neutron star mergers with $r_p/M \in [5, 10]$ and various values of NS spin, finding that for the cases considered, those with $r_p/M \leq 8$ merge on the initial encounter, while those with $r_p/M \geq 9$ go back out on an elliptic orbit after the fly-by. In Figs. 2 and 3 we show sequences of snapshots of the equatorial rest-mass density in order to illustrate the dynamics of some representative cases. In what follows we present several results: in Sec. III A we demonstrate how the NS spin angular momentum can affect the lifetime of the HMNS formed post-merger; in Sec. III B we comment on the effect of spin on the GW signal, both from fly-bys, and from the evolution of the HMNS; and in Sec. III C we explain how the amount of material remaining outside the merger remnant varies with NS spin, and the effect this will have on possible EM transients from such mergers. Finally, in Sec. III D we discuss in detail the one-arm instability arising in the resulting HMNS for a number of cases, including how this affects the post-merger dynamics and GWs from these cases.

A. Prompt collapse versus hypermassive neutron star formation

In agreement with the results in [40], we find that the eccentric NSNS mergers can result either in the prompt formation of a BH, or the creation of a HMNS, and that this outcome depends on the impact parameter. However, here we also find that NS spin can have a significant effect on whether prompt collapse to a BH occurs. In particular, for $r_p/M = 5$ we find that if the NS spins are $a_{\text{NS},i} \lesssim 0.2$, $i = 1, 2$ then prompt collapse to a BH occurs. However, for spins $a_{\text{NS},i} \geq 0.2$ a long lived HMNS forms. In other words, moderately high NS spins can prevent prompt collapse to a BH and prolong the lifetime of the HMNS. In these cases where a HMNS forms, since the total mass of the system is above the supramassive limit, the prompt collapse to a BH is prevented by some combination of thermal energy and centrifugal support. As illustrated in Table II, there is substantial shock heating and in most HMNS cases $\sim 30\%$ of the internal energy is thermal. As also illustrated there, most of the angular momentum of the system remains unradiated. The HMNS cases will eventually undergo delayed

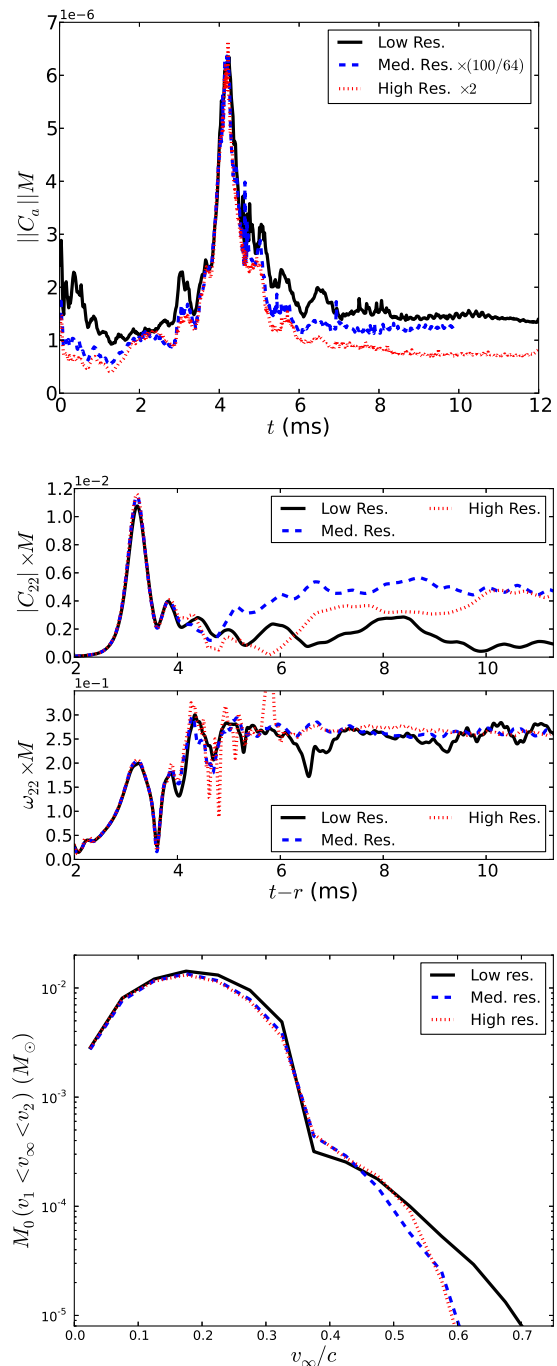


FIG. 1. Resolution study for the case with $r_p/M = 8$ and $(a_{\text{NS},1}, a_{\text{NS},2}) = (0, 0.4)$. The top panel shows the convergence of the $L2$ norm of the constraints $C_a := \square x_a - H_a$, scaled assuming first-order convergence. Before the merger (when there are no shocks) and at latter times, the convergence is closer to second-order. The middle panels show the magnitude and frequency (time derivative of the phase) of the $\ell = m = 2$ component of Ψ_4 . During the turbulent-like post-merger phase, strict convergence of the amplitude of the waveform is lost, though there is still good agreement on the frequency. The bottom panel shows the amount of unbound rest-mass, binned according to the asymptotic velocity, as a function of resolution.

collapse due to some combination of loss of thermal pressure support from cooling [24] and centrifugal support due to magnetic braking of the differential rotation (neither of which we model), as well as GW emission of angular momentum [22].

To probe whether centrifugal support plays a crucial role in the HMNS remnant in the $a_{\text{NS},i} = 0.2$ case we performed a $r_p/M = 5$ run with spins of the same magnitude but antialigned, i.e., $a_{\text{NS},2} = -a_{\text{NS},1} = 0.2$. We find the outcome to be the prompt formation of a BH. Since this configuration has almost the same angular momentum as the $r_p/M = 5$, $a_{\text{NS},i} = 0.0$ case, which also promptly forms a BH, total angular momentum at merger seems to be the determining feature, as opposed to, for example, the different compactness of spinning versus nonspinning NSs. In Fig. 4 we show the fraction of internal energy that is thermal for several of the $r_p/M = 5$ cases. This indicates that for the cases that form HMNSs, most of the thermal energy is generated after the initial merger, and after the time when the lower spin cases have already collapsed to BHs. Once the hot HMNS forms, however, it may be necessary for it to cool [24, 91], as well as lose angular momentum, in order to collapse. The conclusion that centrifugal support is important here is further supported by the $r_p/M = 8$, $a_{\text{NS},1} = a_{\text{NS},2} = -0.4$ case, which despite having more orbital angular momentum than the $r_p/M = 5$ case, also promptly collapses to a BH.

These results demonstrate that following the NSNS merger, NS spin not only can prevent prompt collapse to a BH, but it can also trigger the collapse if the spins are antialigned with the orbital angular momentum. The data listed in Table II suggests that for $M_{\text{NS},i} = 1.35M_\odot$ NSs which are constructed with the HB EOS, these eccentric mergers will form a BH promptly if the initial total angular momentum of the NSNS is below the value $J_{\text{ADM}}/M_{\text{ADM}}^2 \simeq 0.82$. The amount of angular momentum carried off by GWs up until merger for these eccentric mergers is $J_{\text{GW}}/M_{\text{ADM}}^2 \lesssim 0.03$. Thus, the threshold value of the total angular momentum at merger for prompt collapse to a BH is $J_{\text{ADM}}/M_{\text{ADM}}^2|_{\text{thres}} \simeq 0.79$. This demonstrates yet another example where cosmic censorship is generically respected in astrophysical scenarios. Using this threshold value we may predict that for NS spins $a_{\text{NS},i} = -0.06$ for $M_{\text{NS},i} = 1.35M_\odot$ NSs, the $r_p/M = 6$ case will collapse promptly to a BH. We can also use $J_{\text{ADM}}/M_{\text{ADM}}^2|_{\text{thres}}$ to make predictions for quasicircular NSNS binaries. For example, at the termination point for sequences of quasicircular, irrotational NSNSs in quasiequilibrium with compactness $C \geq 0.16$, the ADM angular momentum satisfies $J_{\text{ADM}}/M_{\text{ADM}}^2 \simeq 0.9$ [92]. Thus, spins $a_{\text{NS},i} = -0.2$ for $M_{\text{NS},i} = 1.35M_\odot$ NSs in quasicircular binaries constructed with the HB EOS may trigger prompt collapse to a BH. This is because after adding spins the total angular momentum near the termination point for quasiequilibrium sequences may be $J_{\text{ADM}} \sim 0.9M_{\text{ADM}}^2 - 2 \times 0.2(M_{\text{ADM}}/2)^2 = 0.8M_{\text{ADM}}^2 \sim J_{\text{ADM}}|_{\text{thres}}$, and at merger J_{ADM} will be re-

duced by the amount of angular momentum carried off by GWs. However, careful calculations in full GR are necessary to confirm the above predictions, which we intend to do in the future.

B. Gravitational Waves

Spin also affects the gravitational wave signal, both from the final merger, and to some extent the signal from non-merging close encounters. In Figs. 5 and 6 we show the dominant contribution to the GW signal for some example cases with $r_p/M = 5, 8, 9$, and 10; see also Table II. For $r_p/M = 10$, the first encounter (the only one simulated) is a non-merger fly-by, and the apparent trend is that the higher the initial NS spins, the smaller the amplitude of the GWs during the pericenter passage. This is not unexpected as higher spin implies a less compact neutron star for the same gravitational mass. The fly-by cases also clearly demonstrate that f-mode oscillations are excited following the close encounter. GWs from such f-mode oscillations were first proposed in [93] and analyzed with numerical relativity simulations in [39]. In the cases we study, we find that the higher the initial NS spins, the larger is the initial GW amplitude corresponding to these f-mode oscillations. This is likely due to the fact that the tidal perturbations impose stronger oscillations on less compact stars. The frequency of the f-modes is a weak function of the NS spin (see e.g. [89]) – spin effects seem to become important only for NS spin angular frequencies above $\sim 80\%$ of the Keplerian (mass-shedding) limit. The top panel of Fig. 6 shows one case with $r_p/M = 9$ that undergoes multiple close encounters, exciting large f-mode oscillations, before finally merging and creating a HMNS. Though such cases are more computationally expensive to follow through merger, they will be the more common occurrence among eccentric mergers.

Given the relatively low amplitude and high frequency of the f-mode GW signals, by themselves they may not be readily detectable. However, insofar as they extract energy and angular momentum from the orbit and thus decrease the successive times between primary bursts in a multiple encounter merger, they could be measurable indirectly. We leave it to future work to ascertain how plausible their detectability is, and whether, for example, properties of the EOS or NS spin could be measured via the inferred strength of f-mode excitations.

Figure 5 also demonstrates that there is significant variability in the amplitude and frequency of the GW oscillation modes that arise when a HMNS forms following merger (for $r_p/M = 5, 8$, and 9); see also Fig. 7 where we plot the GW power spectra of several merger cases. It is difficult to extract clear trends on how the various initial parameters influence this variability, in particular given the turbulent-like nature of the post-merger phase, which in turn prevents establishing error bars on some measurable features using convergence studies. However,

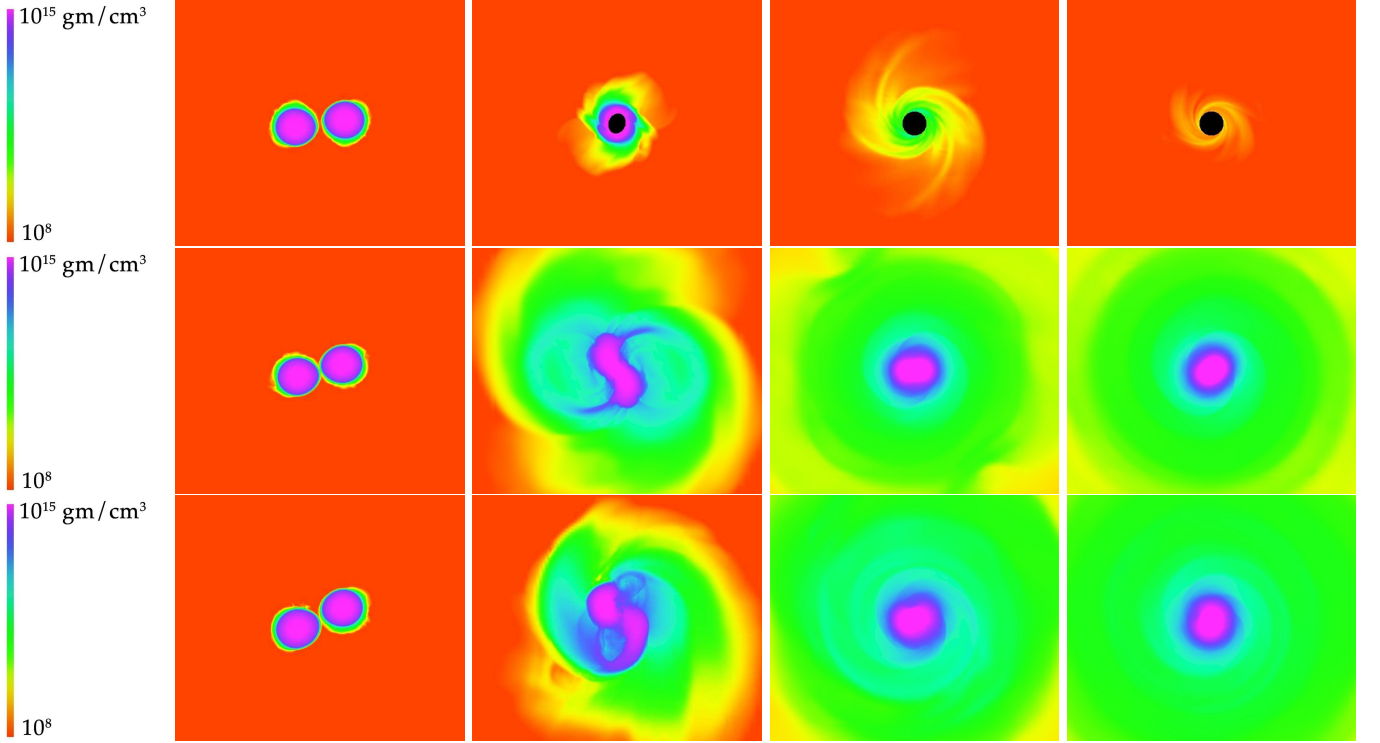


FIG. 2. Equatorial rest-mass density snapshots for representative cases. Top row ($r_p/M = 5$, $a_{\text{NS},1} = a_{\text{NS},2} = 0$) from left to right: ($t \approx 192M \approx 2.6$ ms) the NSs make contact; ($t \approx 216M \approx 2.9$ ms) a BH apparent horizon forms; ($t \approx 246M \approx 3.3$ ms) the BH accretes the small disk; ($t \approx 362M \approx 4.8$ ms) little matter is left outside the BH at the end of the simulation. Second row ($r_p/M = 5$, $a_{\text{NS},1} = a_{\text{NS},2} = 0.2$) from left to right: ($t \approx 192M \approx 2.6$ ms) the NSs make contact; ($t \approx 276M \approx 3.7$ ms) the two cores bounce, launching shocks and ejecting matter outwards; ($t \approx 621M \approx 8.3$ ms) the cores re-coalesce and a HMNS forms with a bar-shaped core surrounded by an extended envelope and disk; ($t \approx 1140M \approx 15.2$ ms) the one-arm spiral instability is not evident. Third row ($r_p/M = 6$, $a_{\text{NS},1} = 0.4$, $a_{\text{NS},2} = 0.0$) from left to right: ($t \approx 197M \approx 2.6$ ms) the NSs make contact (the spinning NS is the star on the left); ($t \approx 270M \approx 3.6$ ms) the two cores bounce while the spinning NS (now on the right) is being disrupted ejecting matter outward; ($t \approx 722M \approx 9.6$ ms) the cores recollapse forming a HMNS with an egg-shaped core, surrounded by an extended envelope and disk; ($t \approx 1165M \approx 15.5$ ms) the one-arm spiral instability is not evident. The radius of each NS prior to merger ($R_{\text{NS}} \approx 12$ km) sets the scale.

in some cases, qualitative properties can be deduced, the most striking of which is when initial conditions lead to a HMNS that is unstable to the $m = 1$, one-arm instability. We elaborate on this aspect of the GW signature below in Sec. III D.

C. Post-merger matter distribution and electromagnetic counterparts

As a general trend, we find that when the NSs are spinning, the amount of matter that is unbound from the system, and hence may power an electromagnetic transient, increases. We list the total rest-mass of the ejecta, along with the mass-averaged velocity, shortly following merger for the various cases in Table II, and for example, for $r_p/M = 5$ the ejecta rest-mass can reach $\sim 0.1M_\odot$ even for moderately high NS spins of $a_{\text{NS}} = 0.2$, which is an order of magnitude more than the corresponding non-spinning case. Similar results hold true for $r_p/M = 8$.

This trend with initial NS spin does not seem to hold for $r_p/M = 6$, as larger initial spin apparently leads to smaller ejecta mass. This may be related to the fact that in the $r_p/M = 6$ case with nonspinning stars, the two NS cores merge and then bounce strongly, ejecting a significant amount of mass. This bounce is weaker in the cases with spin, and as a result matter is ejected only from tidal tails. In that sense, for this particular case spin makes the collision milder.

In the cases where a BH forms promptly after merger, the amount of rest-mass that remains bound and makes up the BH's accretion disk ranges from $10^{-4} M_\odot$ to $3 \times 10^{-3} M_\odot$ in the cases considered here, which is comparable to the amount found in quasicircular NSNS mergers leading to prompt collapse to a BH (see e.g. [96, 97]). Taking the more massive end of this range, and assuming a disk lifetime equal to the average sGRB timescale ~ 0.2 s yields an accretion rate of $\sim 0.005 M_\odot \text{ s}^{-1}$. Further assuming an average conversion efficiency of 1% for converting this to gamma-ray jet luminosity gives

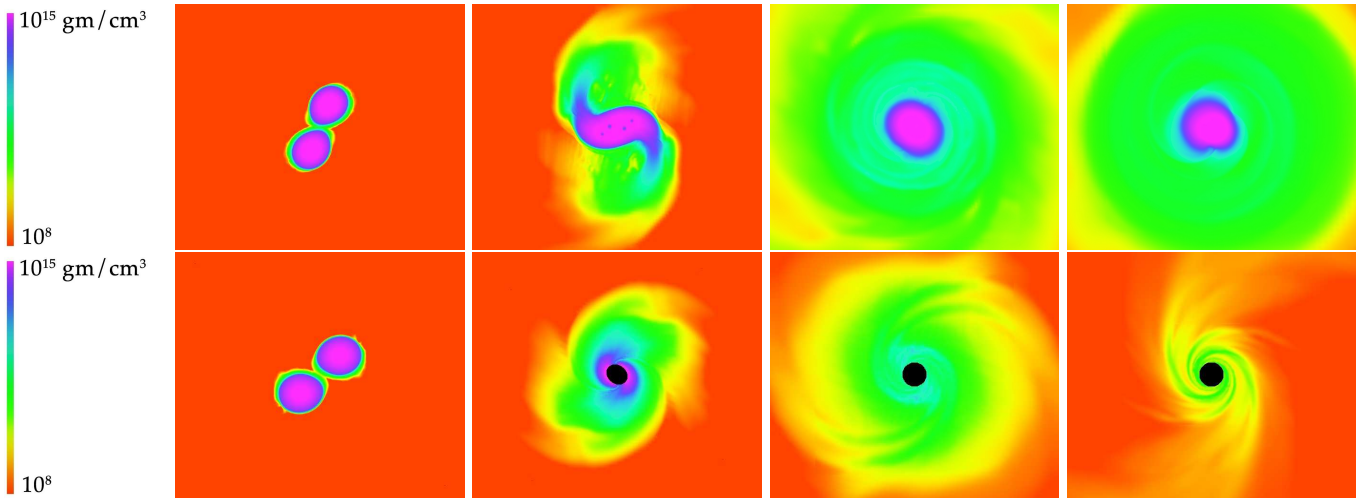


FIG. 3. Equatorial density snapshots for representative cases. Top row ($r_p/M = 8$, $a_{\text{NS},1} = a_{\text{NS},2} = 0.025$) from left to right: ($t \approx 212M \approx 2.8$ ms) the NSs make contact for the first time; ($t \approx 277M \approx 3.7$ ms) the two stars merge, shearing and ejecting matter outward from the outer edges of the two stars; ($t \approx 591M \approx 7.86$ ms) shortly after a HMNS forms with an ellipsoidal core surrounded by an extended envelope and disk; ($t \approx 1160M \approx 15.4$ ms) the one-arm spiral instability develops (see Sec. III D) giving rise to an $m = 1$ deformation. Bottom row ($r_p/M = 8$, $a_{\text{NS},1} = a_{\text{NS},2} = -0.4$) from left to right: ($t \approx 207M \approx 2.8$ ms) the NSs make contact for the first time; ($t \approx 260M \approx 3.5$ ms) an apparent horizon is found for the first time; ($t \approx 288M \approx 3.8$ ms) the BH accretes matter while some matter is ejected; ($t \approx 500M \approx 6.6$ ms) little matter ($\sim 10^{-3}M_\odot$) is left outside the BH at the end of the simulation. The radius of each NS prior to merger ($R_{\text{NS}} \approx 12\text{km}$) sets the scale.

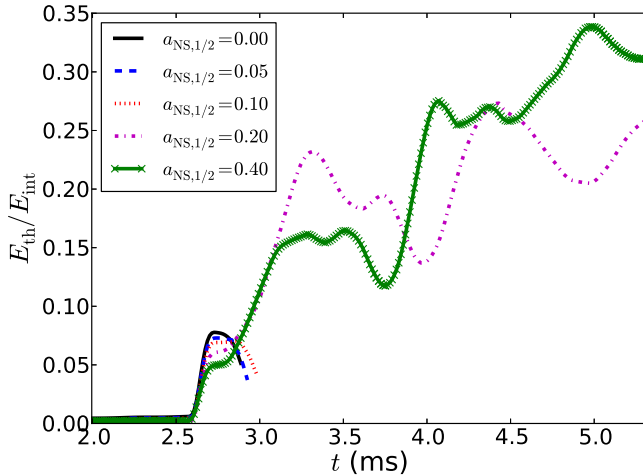


FIG. 4. The fraction of internal energy that is thermal (as measured by an Eulerian observer) as a function of time for cases with $r_p/M = 5$ and various spins. The truncated curves are the cases that promptly collapsed to BHs around merger. For the cases that do not promptly form BHs, most of the heating occurs later in the evolution, after the time when smaller spin cases have already collapsed to BHs.

a sGRB luminosity of 10^{50}erg s^{-1} — on the lower end of observed sGRB luminosities. Typical accretion rates toward the end of the simulations forming BHs are $\sim 0.01\text{--}0.05M_\odot\text{ s}^{-1}$, implying disk lifetimes of up to $\sim 0.1\text{s}$.

However, proper treatment of magnetic fields, which are not accounted for here, and of the resulting magnetohydrodynamic turbulence, are necessary to accurately determine the accretion rate and disk lifetime, and whether jets can be launched from these systems [20, 98].

As evident in Fig. 8, which shows the asymptotic velocity distribution of the unbound matter for $r_p/M = 5$ and 8, there is significant variability of the outcome depending on both the initial NS spin and the periastron distance. In the cases where a BH forms promptly after merger, the amount of unbound material is markedly suppressed. When a HMNS forms, spin also seems to enhance the mass in the high velocity tail of the ejecta. This interesting result may have consequences for EM signatures that may accompany these events. In particular, in [14] it was suggested that ejected, neutron-rich matter traveling at velocities $v \gtrsim 0.5c$ may expand so rapidly that most neutrons may avoid capture (slower moving ejecta will still capture neutrons). As a result free neutron beta-decay may power a potentially observable EM signal with rise time of order a few hours and peaking in the U-band even if the ejecta at such high velocities has a mass as low as $\sim 10^{-4}M_\odot$. The results in Fig. 8 thus suggest eccentric mergers, especially with rapidly spinning NS, may offer favorable conditions for producing EM counterparts powered by free neutron decay.

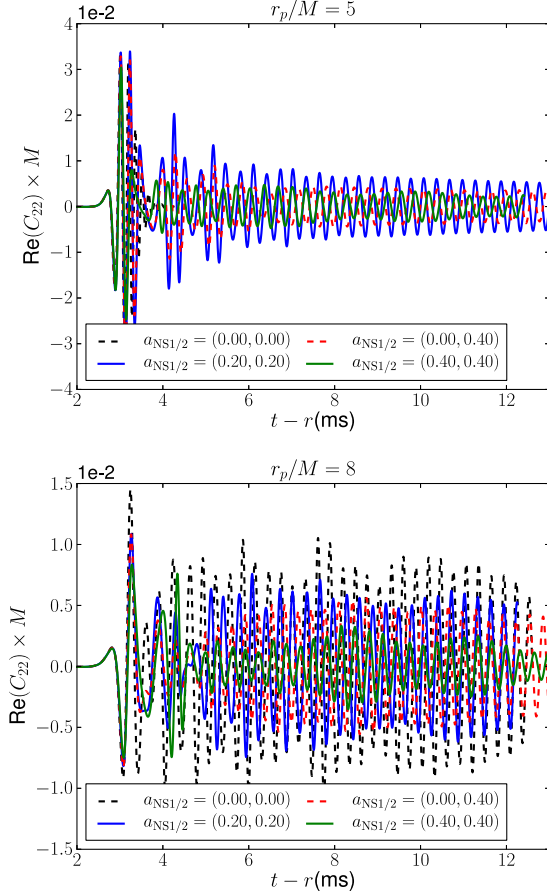


FIG. 5. The $l = m = 2$ mode of the Newman-Penrose scalar Ψ_4 representing the GWs. The top and bottom panels show the real part of Ψ_4 from representative cases with $r_p/M = 5$ and 8, respectively. The notation $a_{\text{NS1}/2} = (A, B)$ implies that spin $a_{\text{NS},1} = A$ and spin $a_{\text{NS},2} = B$. Note the different vertical scale between the two panels.

1. Kilonovae

The increase in the amount of ejected material with increasing NS spin would also enhance the luminosity of a kilonova (also called a macronova) that may occur after merger. Unbound NS material travelling at speeds $v \lesssim 0.5c$ will decompress and may form heavier elements via the r-process. A kilonova results from subsequent fission of the shorter-lived radioactive products of the r-process [99, 100]. Though it was originally thought a typical kilonovae would peak in the optical band [101], recent calculations suggest that because of contributions from the lanthanides, the opacity in the r-process material is much greater than in iron-rich ejecta from supernovae [102, 103], resulting in a dimmer and redder transient that peaks in the infrared. The results of [102]

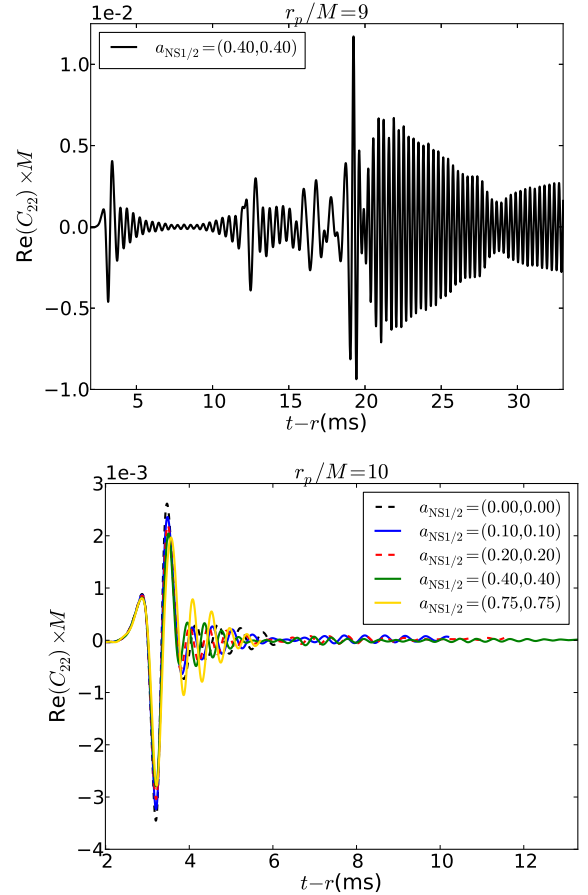


FIG. 6. The $l = m = 2$ mode of the Newman-Penrose scalar Ψ_4 representing the GWs. The top panel show the real part of Ψ_4 of the one $r_p/M = 9$ case studied, and the bottom representative cases from $r_p/M = 10$. The initial encounter in all these examples is a fly-by leading to a bound system, though only for the $r_p/M = 9$, $a_{\text{NS1}/2} = 0.4$ case did we follow the subsequent evolution all the way through merger (here, as indicated by the GW signal, a second fly-by occurs roughly 10 ms after the first, and after that a couple of grazing close encounters before the merger at ≈ 19 ms). The notation $a_{\text{NS1}/2} = (A, B)$ implies that spin $a_{\text{NS},1} = A$ and spin $a_{\text{NS},2} = B$. Note the different vertical and horizontal scales between the two panels.

suggest a rise time of

$$t_{\text{peak}} \approx 0.25 \left(\frac{M_{0,u}}{10^{-2} M_{\odot}} \right)^{1/2} \left(\frac{v}{0.3c} \right)^{-1/2} \text{ d}, \quad (9)$$

measured from the merger, and peak luminosities of

$$L \approx 2 \times 10^{41} \left(\frac{M_{0,u}}{10^{-2} M_{\odot}} \right)^{1/2} \left(\frac{v}{0.3c} \right)^{1/2} \text{ erg s}^{-1} \quad (10)$$

Table II lists these estimates using the corresponding properties from the cases studied here. As can be seen in the table, there is large variation in estimated kilo-

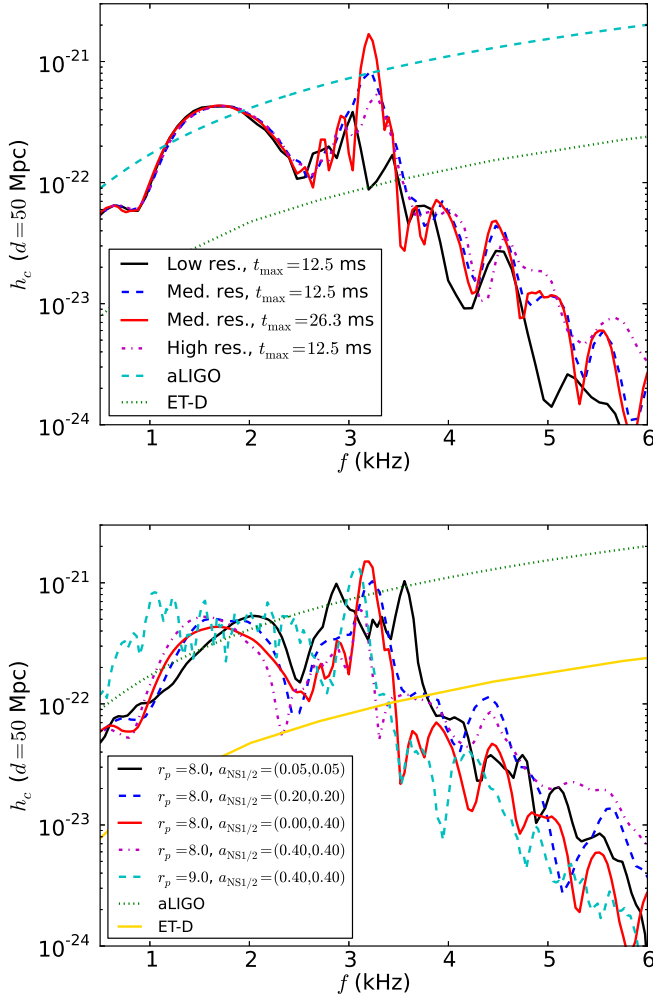


FIG. 7. The characteristic strain, defined as $h_c = |\tilde{h}|f$ where \tilde{h} is the Fourier transform of the strain and f is frequency, as observed at a distance of 50 Mpc and on-axis. In the top panel we show the $r_p/M = 8$, $a_{\text{NS},1} = 0$, $a_{\text{NS},2} = 0.4$ case at the three different resolutions, and, for the medium resolution case, the resulting curve when the waveform is extended from 12.5 to 26.3 ms. In the bottom panel we show various cases with different spins. For comparison, we also show the proposed broad-band aLIGO sensitivity curve [94] and proposed Einstein Telescope (ET-D) sensitivity curves [95].

novae peak timescales and luminosities across the different cases when the NS spin is taken into account. For $r_p/M = 5$, this variation is indirectly attributable to spin insofar as it contributes to prompt BH versus HMNS formation. For $r_p/M = 8$, spin causes variation in these estimated kilonovae properties by a factor of a few over the range simulated, with higher initial spin tending to produce brighter, longer-lived counterparts. Thus the detection of kilonovae from NSNS mergers with spinning NSs may be easier not only because they tend to be brighter, but also because of the longer light curve

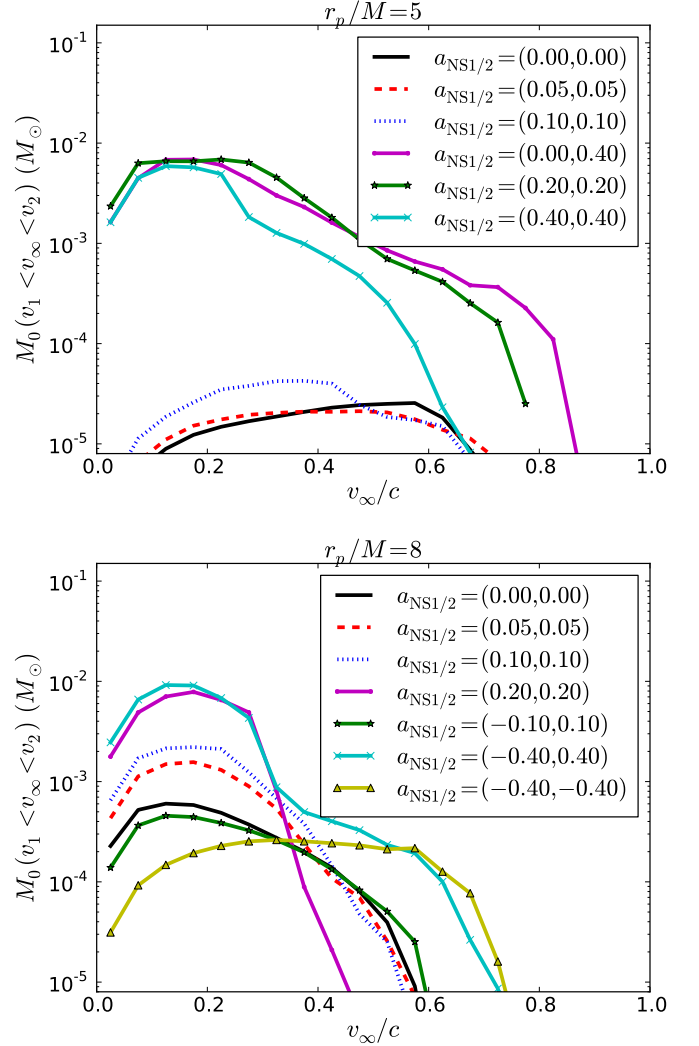


FIG. 8. Distribution of the asymptotic velocity of unbound rest-mass, binned in increments of $0.05c$, and computed ≈ 7.0 ms post-merger for $r_p/M = 5$ (top) and $r_p/M = 8$ (bottom) and various spins.

rise time more events will straddle the observation times of EM surveys. Factors of a few in luminosity could also make the difference between detection and non-detection with planned surveys. For example, an $L \sim 10^{41} \text{ erg s}^{-1}$ kilonova near the edge of LIGO's observable volume (at 200 Mpc) would translate to an r-band magnitude of 23.5 mag [102], i.e., one magnitude above the proposed LSST survey sensitivity.

2. Radio signal from collision with interstellar medium

Another transient proposed to arise from material ejected in compact object mergers is radio emission when this material collides with the interstellar medium

(ISM) [12]. Because of the large amount of kinetic energy and mildly relativistic velocities of the ejecta in these eccentric mergers, such signals will evolve more slowly and require longer surveys to identify them as transients compared to kilonovae or sGRBs. These signals typically peak on timescales [12]

$$t_F \approx 6 \left(\frac{E_{\text{kin}}}{10^{51} \text{ erg}} \right)^{1/3} \left(\frac{n_0}{0.1 \text{ cm}^{-3}} \right)^{-1/3} \left(\frac{v}{0.3c} \right)^{-5/3} \text{ yr} \quad (11)$$

with brightness

$$F(\nu_{\text{obs}}) \approx 0.6 \left(\frac{E_{\text{kin}}}{10^{51} \text{ erg}} \right) \left(\frac{n_0}{0.1 \text{ cm}^{-3}} \right)^{7/8} \left(\frac{v}{0.3c} \right)^{11/4} \left(\frac{\nu_{\text{obs}}}{\text{GHz}} \right)^{-3/4} \left(\frac{d}{100 \text{ Mpc}} \right)^{-2} \text{ mJy}. \quad (12)$$

Here E_{kin} is the kinetic energy of the ejecta, ν_{obs} is the observation frequency, d the distance to source, and we estimate $n_0 \sim 0.1 \text{ cm}^{-3}$ as the approximate density in the cores of GC [53]. As shown in Table II, using the estimates from the simulations gives a time to peak brightness of around a year to a couple of decades, with the luminosity varying by as much as a couple orders of magnitude with spin for a fixed initial impact parameter.

3. R-process element limits on merger rates

Besides powering transients, another potentially observable effect of NS ejecta is the contribution it makes to the abundance of r-process elements [21, 104]. Compact object mergers are an attractive explanation since the other major channel, core-collapse supernovae, has difficulty accounting for observed abundances of heavy elements on its own [105–107]. Dynamically assembled binaries, which merge faster than primordial binaries, may even be required to account for r-process material in carbon-enhanced metal-poor stars [108]. Inverting this argument, the observed heavy element abundances can be used to place limits on merger rates as in [53] (though it should be noted that these are strictly applicable only to the early universe and not necessarily relevant for predicting GW event rates). The average r-process production rate of $\sim 10^{-6} M_{\odot} \text{ yr}^{-1}$ [109] per galaxy limits the most extreme cases like the $r_p/M = 8$, $a_{\text{NS},1} = a_{\text{NS},2} = 0.75$ with $M_{0,u} \approx 0.2 M_{\odot}$ to at most $\sim 5 \times 10^{-6} \text{ yr}^{-1}$ per galaxy. Though as the NS spins are unlikely to be near maximal in these mergers, if we assume that a typical eccentric merger with spinning NSs will have $a_{\text{NS},i} = 0.1$, then the ejecta masses are of order $0.01 M_{\odot}$, and the implied merger limits of $\sim 10^{-4} \text{ yr}^{-1}$ are comparable to the predicted rates for primordial NSNS mergers [110].

TABLE III. Frequency $f_{m=1}$, saturation time t_{sat} (measured from the time of merger until the mode dominates over the $m = 2$ mode), and growth time $\tau_{m=1}$ (time it takes for the mode to grow from $1/4$ to $1/2 \times$ its saturation amplitude) of the one-arm spiral mode for various $r_p/M = 8$ cases. Also listed are the dominant frequencies of the $m=2$ ($f_{m=2}$) and $m=3$ modes ($f_{m=3}$). The results are from the high-resolution runs. Apart from the zero-spin case (for which the low resolution run collapsed to a BH), the maximum fractional difference in the saturation time among the different resolutions is 30% (occurring for the $a_{\text{NS},1} = 0.025$, $a_{\text{NS},2} = 0.05$ case), which may serve as a conservative error bar for these calculations. The measurement of the growth rate is noisier and differs by up to a factor of 2 in some cases (see also Fig. 18). The maximum fractional difference in the frequency of the $m = 1$ mode among the different resolutions is 3%.

$a_{\text{NS},1}$	$a_{\text{NS},2}$	t_{sat}	$\tau_{m=1}(\text{ms})$	$f_{m=1}$	$f_{m=2}$	$f_{m=3}(\text{kHz})$
0.000	0.000	19.5	2.0	1.77	3.53	5.24
0.025	0.025	9.9	2.0	1.74	3.47	5.15
0.025	0.050	7.4	1.2	1.72	3.44	5.11
0.050	0.050	10.7	1.2	1.75	3.37	5.24
0.050	0.075	6.2	0.8	1.75	3.27	5.19

D. One-arm spiral instabilities

An unexpected feature we find in the runs with total dimensionless angular momentum at merger of $J_{\text{ADM}}/M_{\text{ADM}}^2 \sim 0.9 - 1.0$, and without a strong disparity in the spins of the two merging NSs, is that the HMNSs that form following merger are subject to the one-arm ($m = 1$) spiral instability, first discovered in [70] for soft EOSs in Newtonian hydrodynamic simulations. We find growing $m = 1$ modes in cases involving lower eccentricities and higher spins as well, but the one-arm instability does not develop there in the sense that the $m = 2$ azimuthal density mode remains greater until termination of these simulations. The one-arm spiral instability was first reported to occur in binary neutron star mergers in [69], and here we expand upon the results presented there, elaborating further on the features of the instability as it takes place in our eccentric NSNS mergers, and including additional cases. We describe the onset, growth, and saturation of the instability following the merger (Sec. III D 1); detail how the matter dynamics are imprinted on the GW signal (Sec. III D 2); show that these results are consistent with the instability developing near the corotation radius (Sec. III D 3); and measure the ratio of kinetic to potential energy, commenting on why these cases do not seem to be dominated by the bar mode (Sec. III D 4). We also present resolution study results (Sec. III D 5); and speculate on the effects of different NS EOSs (Sec. III D 6) and magnetic fields (Sec. III D 7), which we do not include in these simulations.

1. Matter Dynamics

The dynamics during the development of the instability is similar in all cases where it was observed by the termination of our simulations, i.e. for $r_p/M = 8$ and spins $(a_{\text{NS},1}, a_{\text{NS},2}) = (0.0, 0.0)$, $(0.025, 0.025)$, $(0.05, 0.05)$, $(0.025, 0.05)$, $(0.05, 0.075)$ and $(0.1, 0.1)$ and for $r_p/M = 6$ and spins $(a_{\text{NS},1}, a_{\text{NS},2}) = (0.4, 0.4)$. Interestingly, these cases have total angular momentum at merger $J_{\text{ADM}}/M_{\text{ADM}}^2 \sim 0.9 - 1.0$ and this part of the parameter space is relevant for quasicircular NSNSs, too. Results from the $a_{\text{NS},1} = a_{\text{NS},2} = 0.05$ case were presented in [69], though we recall them here for completeness. In Figs. 9 and 10 we show equatorial density and vorticity snapshots from the $r_p/M = 8$, $a_{\text{NS},1} = a_{\text{NS},2} = 0.025$ and $a_{\text{NS},1} = 0.05$, $a_{\text{NS},2} = 0.075$ cases, respectively. The snapshots from these cases demonstrate the dynamics involved, and are representative of symmetric and asymmetric initial spins, respectively. As in [69], we find that the instability seems to be correlated with the generation of vortices near the surface of the HMNS that form due to shearing between the surface and the spiral arms (second row in Figs. 9 and 10). These vortices then spiral in toward the center of the star and create an underdense center. In other words, from the turbulent-like environment following merger a toroidal HMNS forms, i.e., a HMNS whose maximum density does not reside at its center of mass, something that it was argued in [71] is necessary for the one-arm spiral instability to operate.

The rotating one-arm spiral nature of the feature that develops in the HMNS is evident in Fig. 11, which shows several snapshots of the phase of the $m = 1$ mode. Specifically, we plot the curve given by $x + iy = \varpi C_1(\varpi, 0)/|C_1(\varpi, 0)|$ at select times, where the azimuthal modes $C_m(\varpi, z)$ were defined in Eq. (1). These curves essentially show a density-weighted average angle of the location of the $m = 1$ density pattern as a function of the cylindrical radius in the star. If there exists a uniformly-rotating, high-density pattern in the star, it will make these curves appear as a straight lines. This is precisely seen in Fig. 11 for $\varpi \lesssim 2M$. A new feature of this instability that has been not reported before is that the spiral part of the phase of the $m = 1$ mode switches between pointing counterclockwise for a few rotation periods to clockwise for another few rotation periods and back. However, it does not appear that this alternating pattern has a specific period. The feature can be seen by noting that the spirals in the upper left panel in Fig. 11 point counterclockwise, while they point clockwise in all other plots in this figure. Although we have observed some correlation between modulations in the GWs and the times at which the spiral alternates, the correlation is not perfect and we have not been able to assign further physical significance to the feature. In all likelihood the spiral is due to shearing between the inner and outer layers in the star and hence the feature may be important when magnetic fields are accounted for.

Figure 12 shows the amplitude $|C_m|$ [see Eq. (2)] of the

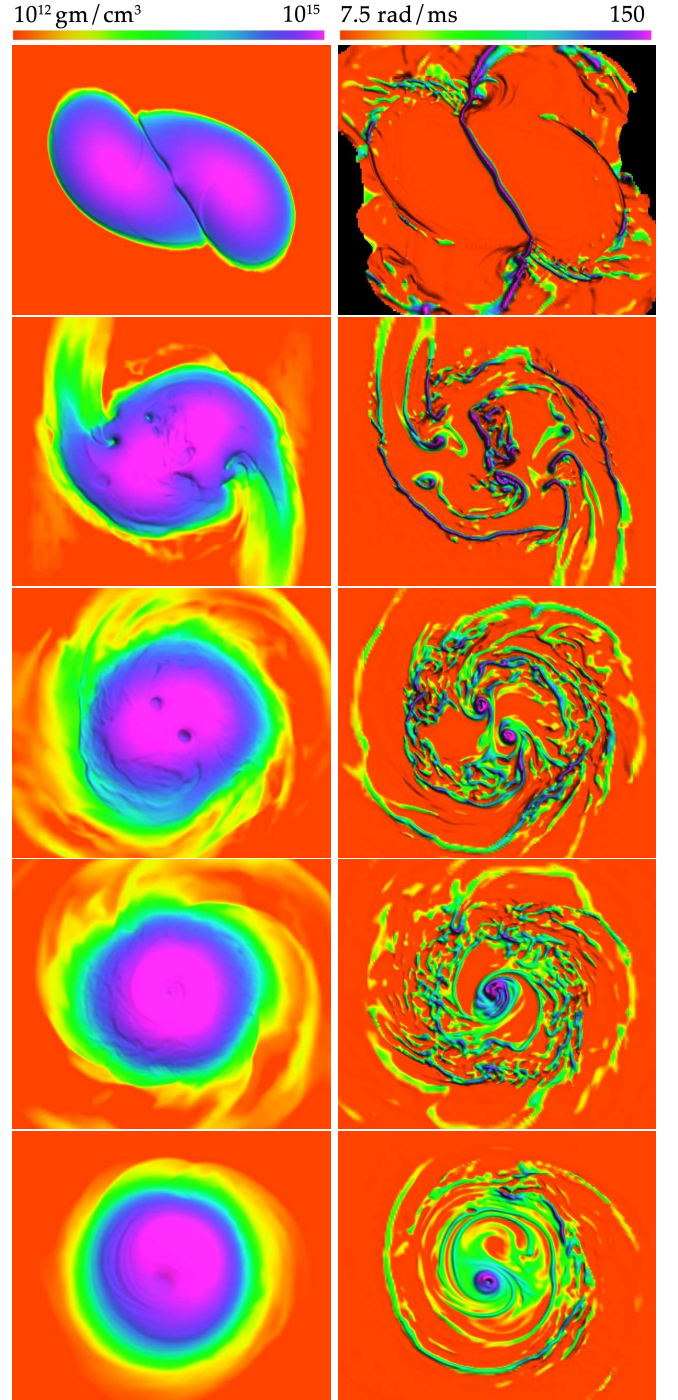


FIG. 9. Equatorial density (left) and Ω_{xy} (right) snapshots at select times for $r_p/M = 8$, $a_{\text{NS},1} = a_{\text{NS},2} = 0.025$. From top to bottom, at $t \approx 3.1$ ms the collision of the NSs creates a vortex sheet at the shear interface that subsequently breaks apart into multiple small scale vortices. Most notably, two larger vortices form near the surface of the star due to shearing between the HMNS and the tidal tails, evident to the left and right of center on the snapshots in the second row ($t \approx 4.5$ ms). At $t \approx 5.5$ ms these two vortices are in the process of migrating towards the center, while other smaller vortices are stretched away. By $t \approx 6.5$ ms the two vortices have merged into one central vortex, giving rise to an underdense rotation axis. The one-arm instability then sets in, and by $t \approx 14.6$ ms it is fully developed, with the vortex now off-set from the center and co-rotating about it.

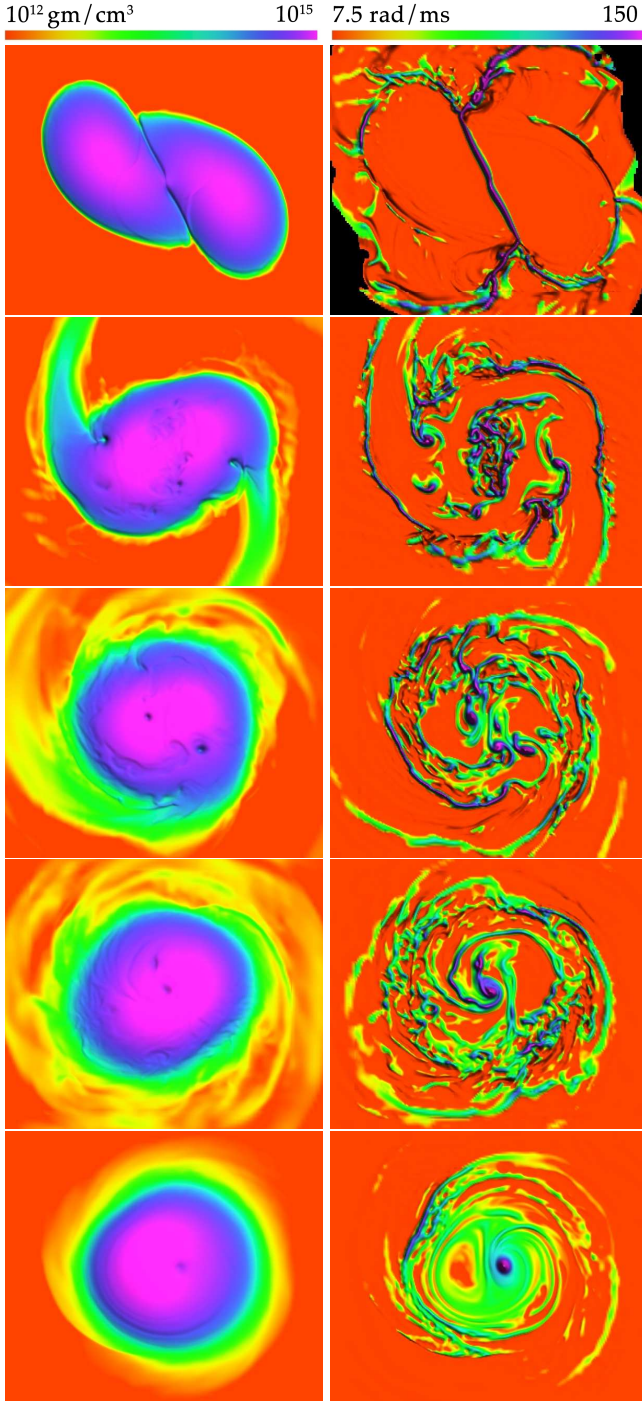


FIG. 10. Equatorial density (left) and Ω_{xy} (right) snapshots at select times for $r_p/M = 8$, $a_{\text{NS},1} = 0.05$, $a_{\text{NS},2} = 0.075$. The description is similar to that in the caption of Fig. 9, and from top to bottom the corresponding coordinate times are the same. Some of the main differences with the symmetric spin case are: a) while both of the larger vortices inspiral toward the center of the HMNS, only one of them reaches the center to create a central underdensity, whereas the other one is stretched out and eventually dissipates as are the other smaller scale vortices; b) in this asymmetric case the vorticity is overall slightly larger throughout the star.

first four density modes for various cases. For the cases where we observe the one-arm spiral instability (top two rows), the plots demonstrate that the power in the $m = 1$ mode ultimately dominates over all other modes, even though the higher m modes are non-negligible. The bottom row in Fig. 12 shows the amplitude of the density modes corresponding to the $r_p/M = 5$ and $r_p/M = 9$ cases. The $r_p/M = 5$ plot is representative of our findings for larger initial NS spins or larger asymmetries at merger; the $r_p/M = 9$ case is the only one we followed through several close encounters, and hence it has less eccentricity at merger than the other cases. In particular, in these two examples we find growing $m = 1$ modes but they do not dominate over the other modes or may require a very long time for this to occur, perhaps even longer than the timescale to collapse. For the $r_p/M = 8$ case with the next highest spin, $a_{\text{NS},1} = a_{\text{NS},2} = 0.1$ (not shown), the $m = 1$ mode begins to dominate over all other $m \neq 0$ modes at $t \approx 31$ ms.

From the plot of $|C_1|$ we can estimate the growth timescale of the instability in the cases where the $m = 1$ mode becomes dominant, and from the Fourier transform of C_1 we can determine the frequency of the mode. In Table III, we list the dominant frequency of the $m = 1$ mode, the amount of post-merger time it takes for this mode to grow to saturation, and the dominant frequencies of the $m = 2$ and $m = 3$ modes for the different cases. The characteristic frequency of the $m = 1$ mode is ~ 1.75 kHz and the time to saturation of order 10 ms. The higher m modes have characteristic frequency that is $\approx m$ times this, which is to be expected if the densest region of the star that contributes most to the mode integrals is rigidly rotating. The $m = 1$ mode frequency is approximately independent of the initial NS spin. It is more challenging to deduce how the growth rate may depend on the initial NS spin, in particular because in the symmetric cases the $m = 1$ mode is entirely seeded by truncation error. Moreover, it seems that the total angular momentum at merger seems to be a more important parameter for determining the time it takes for the $m = 1$ mode to grow above the $m = 2$ mode in magnitude. However, it appears that small $m = 1$ asymmetries shorten this time interval.

2. Gravitational Waves

For all the cases which develop strong $m = 1$ density modes, there is a corresponding contribution to the GW signal, as can be seen in Fig. 13. After merger, mirroring the growth of the $m = 1$ mode in the density, the $m = 1$ component in the GW grows and eventually saturates, though the $(\ell, m) = (2, 2)$ component makes up the dominant contribution to the GW signal throughout the time of the simulations. In the cases where the $m = 1$ mode dominates, the frequencies of the GW modes are $\sim f_m$, and again are given by $\sim m \times f_1$. This can be seen in Fig. 14, which shows the post-merger GW spectrum

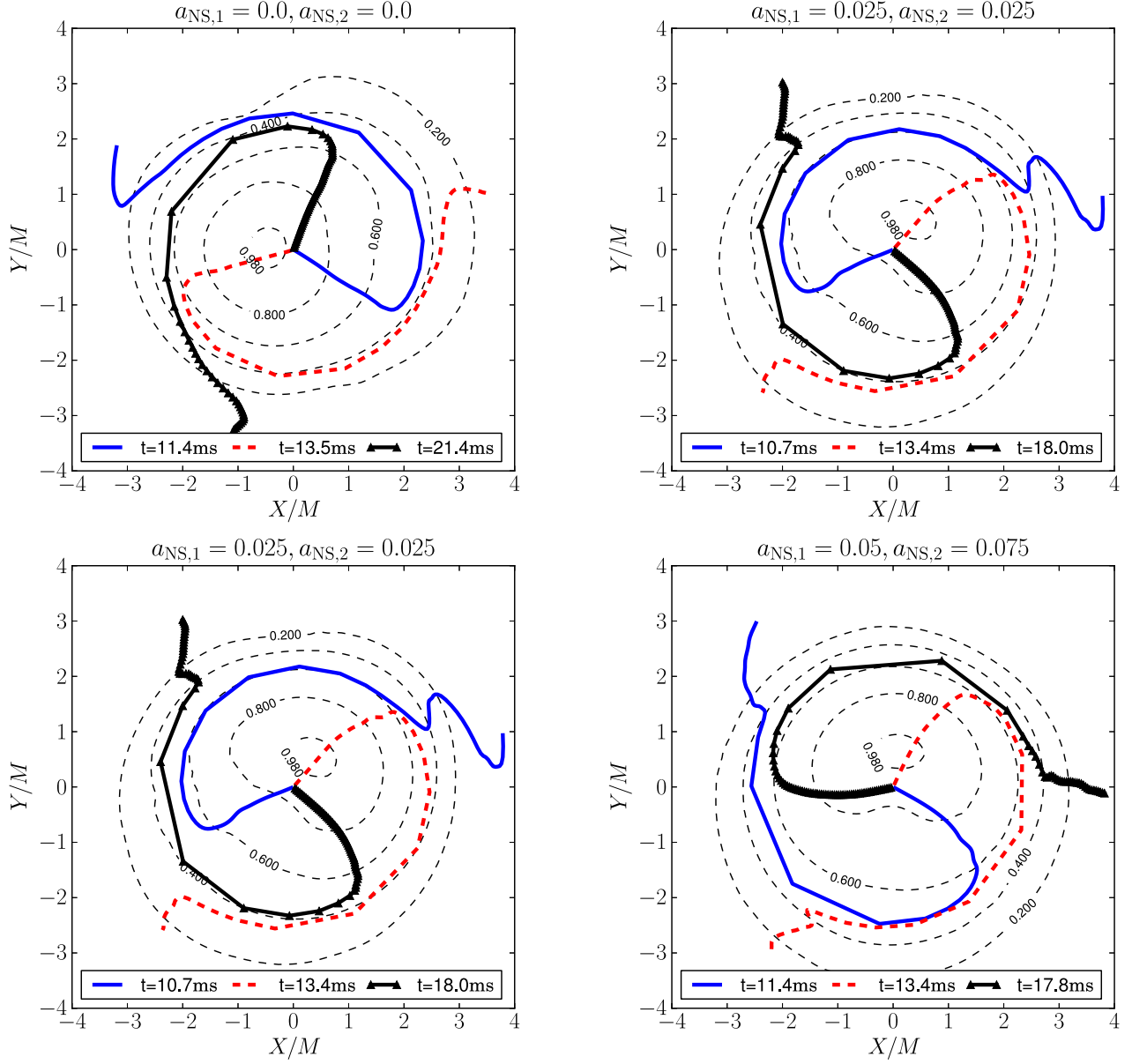


FIG. 11. The phase of C_1 (thick lines) as a function of ϖ in the equatorial plane and center of mass frame for four low-spin $r_p/M = 8$ cases. In each plot the early time chosen corresponds to the growth phase of the instability, the intermediate time is near the time of saturation of the $m = 1$ mode, and the late time is after the $m = 1$ mode dominates over the $m = 2$ mode. For $\varpi/M \lesssim 1.5M$ the pattern of the mode exhibits almost rigid-like rotation, with the characteristic spiral feature evident at larger radii. Overlaid on these plots are equatorial density contours (thin dashed lines) at the time of the intermediate-time phase line, normalized to the maximum density value at that time. The numbers inlined in the contours indicate the value of the level surface. All plots use data from the high-resolution runs.

for the four $r_p/M = 8$ cases that undergo the one-arm spiral instability. Though there is less GW power in the $m = 1$ mode (at ~ 1.7 kHz) than the $m = 2$ mode (at ~ 3.1 kHz), the detectability of the $m = 1$ mode is helped by the fact that ground-based GW detectors like Advanced LIGO will be more sensitive to lower frequencies. Moreover, as is apparent in Fig. 13, the amplitude of the $m = 1$ mode is roughly constant in the latter part

of the simulations and therefore could contribute over a time period much longer than the approximately 15 ms that was integrated over for Fig. 14, as long as conditions favoring the instability persist — in particular the HMNS does not collapse. For the particular cases with $r_p/M = 8$ considered here, except in one low resolution case, none of the HMNSs collapsed during the span of the simulation. We can estimate the additional time it

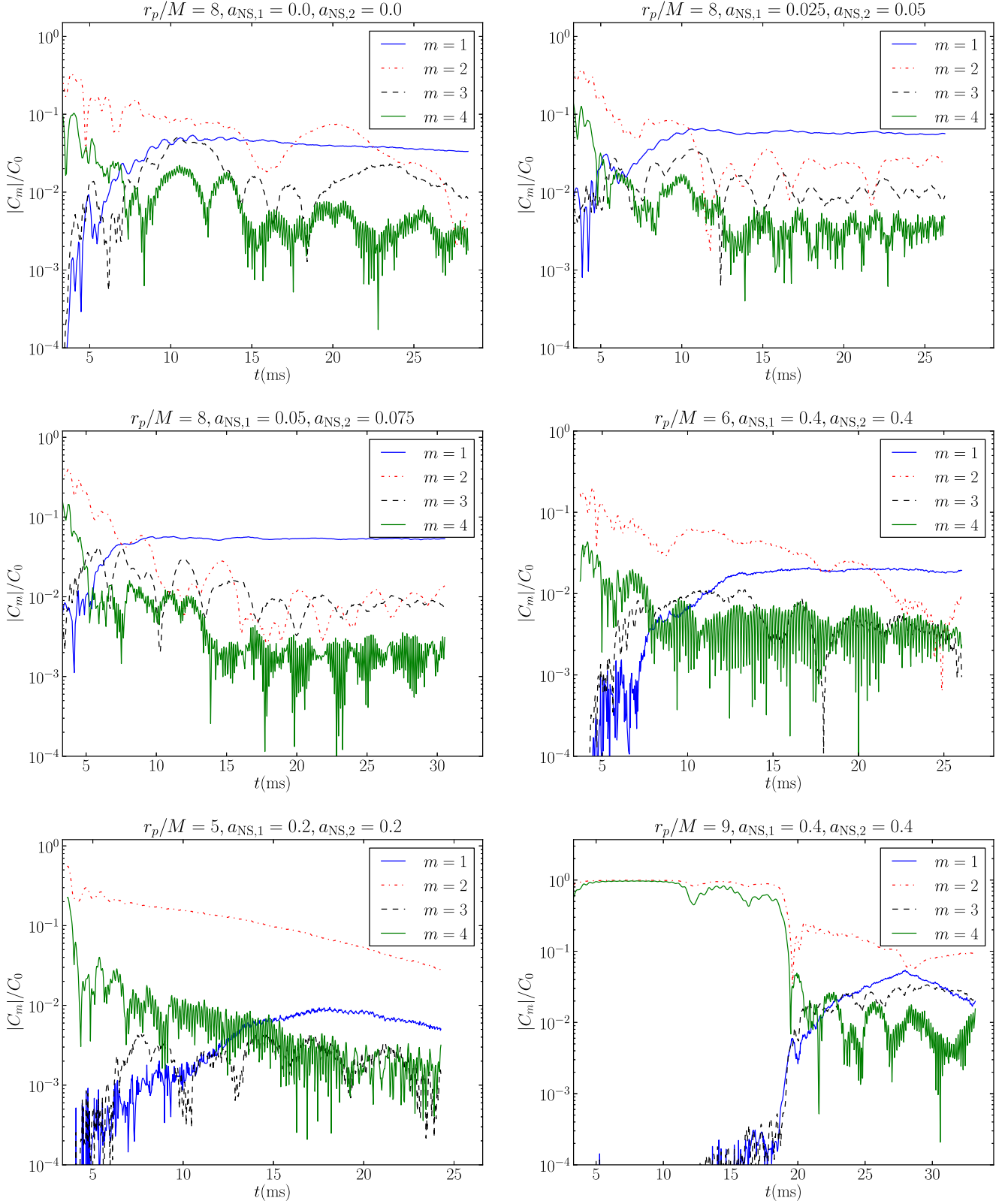


FIG. 12. Amplitude of C_m normalized to C_0 for various cases. The two top rows correspond to low-spin $r_p/M = 8$ cases and a high spin $r_p/M = 6$ case where the $m = 1$ dominates over all other $m \neq 0$ modes by the termination of the simulations. The bottom row corresponds to an $r_p/M = 5$ (left) and $r_p/M = 9$ case (right). The $r_p/M = 9$ case is the one that we followed through several close encounters before merging. After merger the $m = 1$ mode grows for $r_p/M = 5$ and $r_p/M = 9$, but unlike the other cases it never dominates over the $m = 2$ mode by the end of the simulations. The merger time in the $r_p/M = 5$, $r_p/M = 6$ and $r_p/M = 8$ cases is ~ 3.0 ms, whereas it is ~ 18.0 ms in the $r_p/M = 9$ case. Plots corresponding to $r_p/M = 8$ use data from the high-resolution runs.

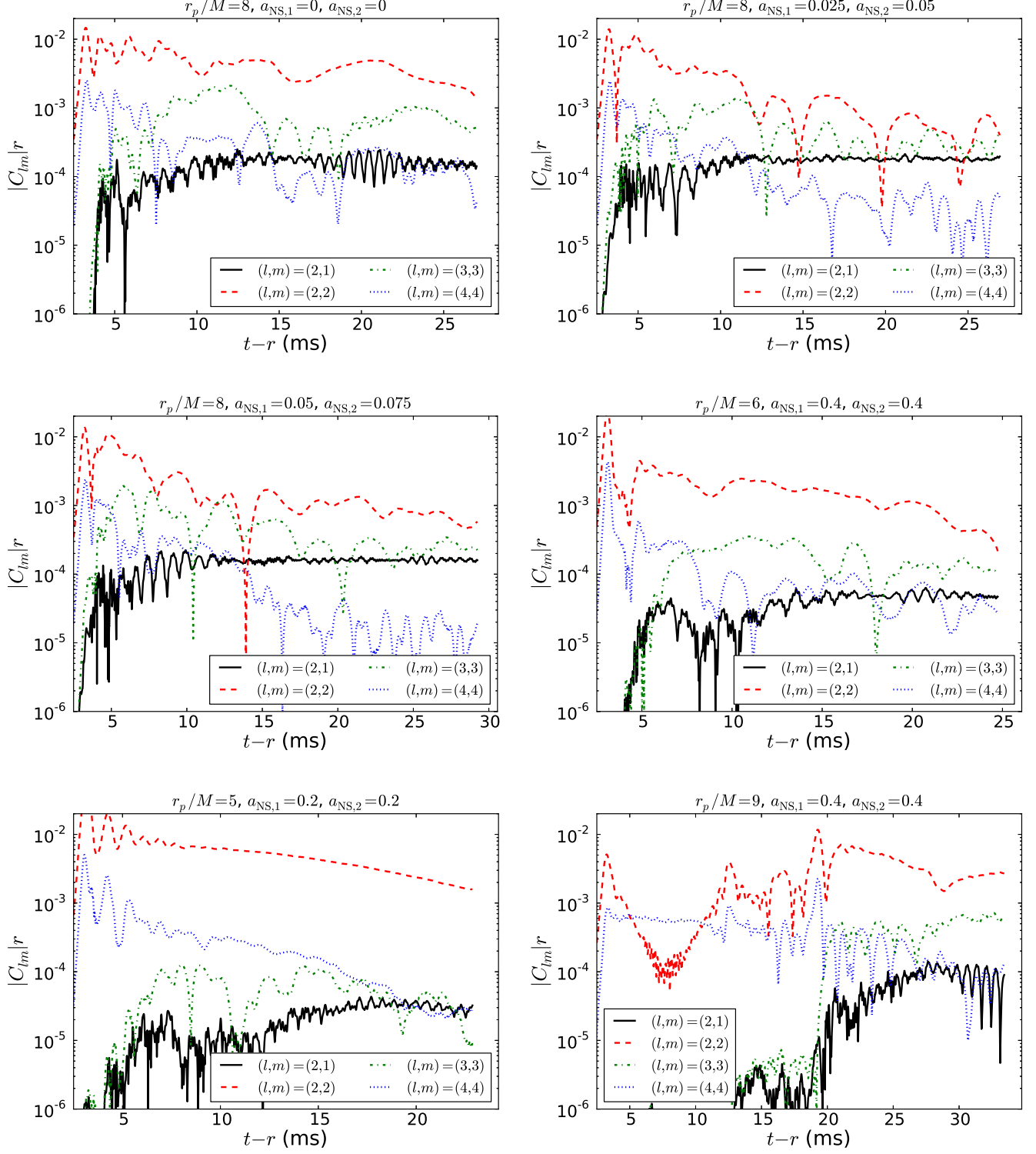


FIG. 13. Amplitude of several spherical harmonic components of the GW signal for various cases following merger. These correspond to the same cases shown in Fig. 12. The $r_p/M = 5$, $r_p/M = 6$ and $r_p/M = 8$ cases merge at $t - r \sim 3.0$ ms, while the $r_p/M = 9$ case merges at $t - r \sim 18.0$ ms. Plots from the $r_p/M = 8$ cases show data from the high-resolution runs.

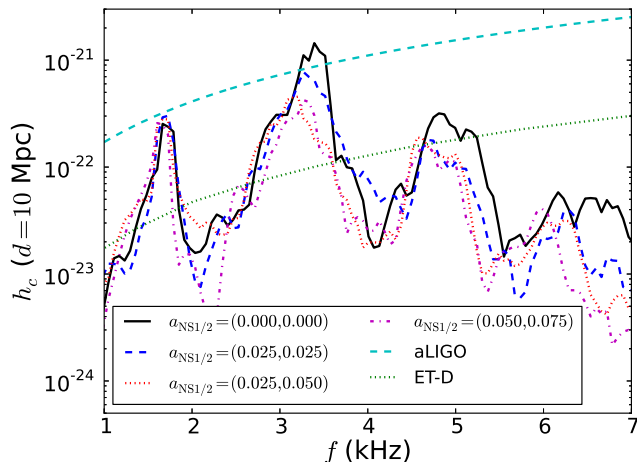


FIG. 14. Characteristic strain of a portion of the GW signal beginning at $t \approx 10$ ms, after the onset of the one-arm instability, and lasting for ~ 15 ms, as would be seen by an edge-on observer (in contrast to the on-axis signal shown in Fig. 7). Shown are various low spin cases with $r_p/M = 8$, as well as the aLIGO and proposed Einstein Telescope (ET-D) sensitivity curves [95] at a distance of 10 Mpc. The HMNS and the one-arm instability GW signal presumably last much longer than the 15 ms represented here (possibly on the order of $t_{\text{HMNS}} \sim 0.1\text{--}1$ s) in which case the GW power would be multiplied by $t_{\text{HMNS}}/(15 \text{ ms})$, and the SNR for this part of the signal by roughly the square root of this factor.

will take for a HMNS to radiate away its remaining angular momentum by taking the difference between the total angular momentum and the amount radiated away in GWs at the end of the simulation, and dividing by the rate at which angular momentum is being lost at that time; this gives times ranging from 0.4–3 s for the cases considered here. On these timescales, other physical effects like cooling due to neutrino emission and magnetic braking of the differential rotation (neither of which we model here) will be important in determining the collapse time of the HMNS. Nevertheless, it is not unreasonable to expect that the integrated power in the mode could end up being one to two orders of magnitude larger than shown in Fig. 14, as simulations have shown that at least in some cases HMNSs may survive for up to ~ 3 s [91].

3. HMNS angular velocity and corotation radius

As first pointed out in [72], and later also argued in [73], stellar shear instabilities, such as the one-arm spiral instability, develop near the corotation radius. The results we find are consistent with this interpretation but here for hot, differentially rotating HMNSs that form following NSNS mergers.

In the left panel of Fig. 15 we plot the azimuthally averaged angular velocity profile of the HMNS at se-

lect times, including the angular frequency Ω_1 of the $m = 1$ mode. We show results from the $r_p/M = 8$, $a_{\text{NS},1} = a_{\text{NS},2} = 0.025$ case which are representative for the low-spin cases developing the one-arm spiral instability. The plot shows that after HMNS formation, and for times prior to the development of the one-arm spiral instability, the HMNS has a high-degree of differential rotation. Assuming that Ω_1 is a good approximation to the oscillation frequency of the unstable mode, the figure also demonstrates that there exists a corotation radius, i.e., a radius at which the local angular velocity of the fluid matches the frequency of the $m = 1$ mode. This result extends earlier criteria for the development of shear instabilities from isolated cold stars to hot HMNSs formed in the NSNS mergers.

Following the development of the $m = 1$ instability, the angular velocity profile of the star changes such that for $0.5M \lesssim \varpi \lesssim 1.5M$ the local angular velocity of the fluid is approximately constant and matches the pattern speed of the $m = 1$ mode, which explains the almost perfect rigid rotation of the $m = 1$ density pattern we observe in our simulations. For $\varpi \gtrsim 1.0M$ we find that the angular velocity falls off roughly like a shallow power law: $\Omega \propto \varpi^{-0.29}$.

4. Kinetic to Potential Energy Ratio

For these cases, we also measure the ratio of kinetic to potential energy given in Eqs. (4)–(6), in particular as an indication of possible susceptibility to a bar mode instability. This is shown in the top panel of Fig. 16. Since the fractional difference between T_{rot} and T_{kin} in all cases we study here is less than 2%, we plot $T_{\text{kin}}/|W|$ as an upper limit. These plots indicate that after the HMNSs settle from the violence of the merger (at $t \simeq 600M$) the stars have a high value of $T_{\text{kin}}/|W|$, but smaller than the critical value of $\simeq 0.26$ which is usually quoted as being necessary for the development of the high- $T/|W|$ dynamical bar mode instability, see e.g. [23, 88, 89] and references therein. The observed trend is that for symmetric spins, the higher the initial NS spin the larger the value of $T_{\text{kin}}/|W|$. Our cases with asymmetric spins (which already have a small $m = 1$ asymmetry) lead to slightly larger $T/|W|$. It is also interesting that the $a_{\text{NS},1} = a_{\text{NS},2} = 0.05$ case has a smaller value of $T/|W|$ than the $a_{\text{NS},1} = 0.025$, $a_{\text{NS},2} = 0.05$ case, although the former has slightly larger initial angular momentum. Related to this, the bottom panel of Fig. 16 shows that following merger the initially symmetric spin cases lose more angular momentum in GWs than the asymmetric ones, and hence tend to lower $T/|W|$ configurations. This could be due to the fact that the instability develops earlier if a small initial $m = 1$ asymmetry is present and that the net GW signal becomes weaker following the development of the instability as demonstrated, e.g. by the amplitude of the GWs shown in Fig. 13.

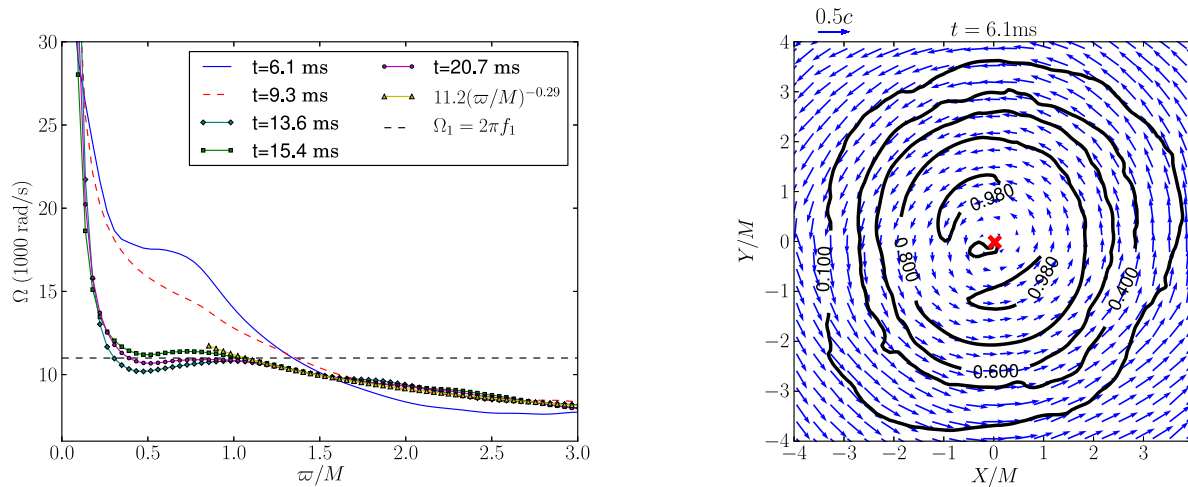


FIG. 15. Left: Azimuthally averaged angular velocity versus the cylindrical coordinate radius. The quantities are computed in the HMNS center of mass at select times. Lines without (with) markers correspond to times prior to (following) the development of the one-arm spiral instability. Also shown are a curve $\propto \varpi^{-0.29}$ which approximates the angular velocity profile for $\varpi \gtrsim 1.0M$, and the angular velocity Ω_1 of the $m = 1$ spiral mode. Right: the arrows indicate the flow coordinate velocity and the black solid lines are contours of density normalized to its maximum value. The contour near the center of the image corresponds to a value of 0.98. The (red) “x” indicates the HMNS center of mass. The plot corresponds to the $t = 6.1$ ms curve shown on the left. The data for both plots are taken from the $r_p/M = 8$, $a_{\text{NS},1} = a_{\text{NS},2} = 0.025$ case.

5. Resolution study

To confirm that the instability is robust with resolution we performed all the cases in Table III using the low, medium and high resolutions also used in the $r_p/M = 8$, $a_{\text{NS},1} = 0.0$, $a_{\text{NS},2} = 0.4$ resolution study. We find that for all cases the development of the one-arm spiral instability occurs at all three resolutions, except for the low resolution $r_p/M = 8$, $a_{\text{NS},1} = 0.0$, $a_{\text{NS},2} = 0.0$ case, where $m = 1$ modes clearly grow, but a BH forms before the instability fully develops. We were not, however, able to formally show convergence for these runs. This is most likely due to the fact that with increasing resolution we observe vortices that form at smaller and smaller scales following merger, and it is difficult to obtain convergence in such turbulent-like environments. However, we find qualitative consistency with increasing resolution of the growth time and early saturation amplitude of the $m = 1$ density modes, as indicated in Figs. 17 and 18. We plan to explore higher resolutions in future analysis of these instabilities.

6. Speculation on Constraining the EOS

Whether or not the one-arm spiral instability develops, and if it does, how long it persists, will depend on how long the HMNS lives before collapsing to a BH. This timescale depends on the EOS, the masses of the NSs, the orbital eccentricity, and the neutron star spins. Given that for many EOSs and for typical NS masses the HMNS

remnant may not survive for more than ~ 20 ms following merger, it may be that a small, but non-negligible neutron star spin, as well as small initial $m = 1$ asymmetries, may be necessary to excite the instability for a relevant range of NS masses. On the other hand it may be that the instability does not develop below a threshold mass or for certain equations of state. If the instability develops for some EOSs and not others, then the instability and the accompanying GWs that may be detected could prove powerful probes of the nuclear EOS. Also, the frequency of the $l = 2$, $m = 1$ mode of the GWs corresponding to the one-arm spiral mode is likely to depend on the EOS much like other post-merger oscillation modes do [29, 68, 111–114]. If so, uncovering correlations between the frequency of the one-arm spiral GW frequency and the EOS could also help constrain the nuclear EOS.

7. Magnetic fields

To assess the potential impact of magnetic fields on the development of the one-arm spiral instability, we need to know how fast the magnetic fields grow from a realistic value of $\sim 10^{10}$ G for a pre-merger NS, to equipartition levels. Although we do not model magnetic fields in our study, we can estimate their amplification timescale, and discuss their impact.

Magnetic fields in NSNS mergers can be amplified by various processes including turbulence arising at the NS-NS shear/colliding interface [115], and the magnetorota-

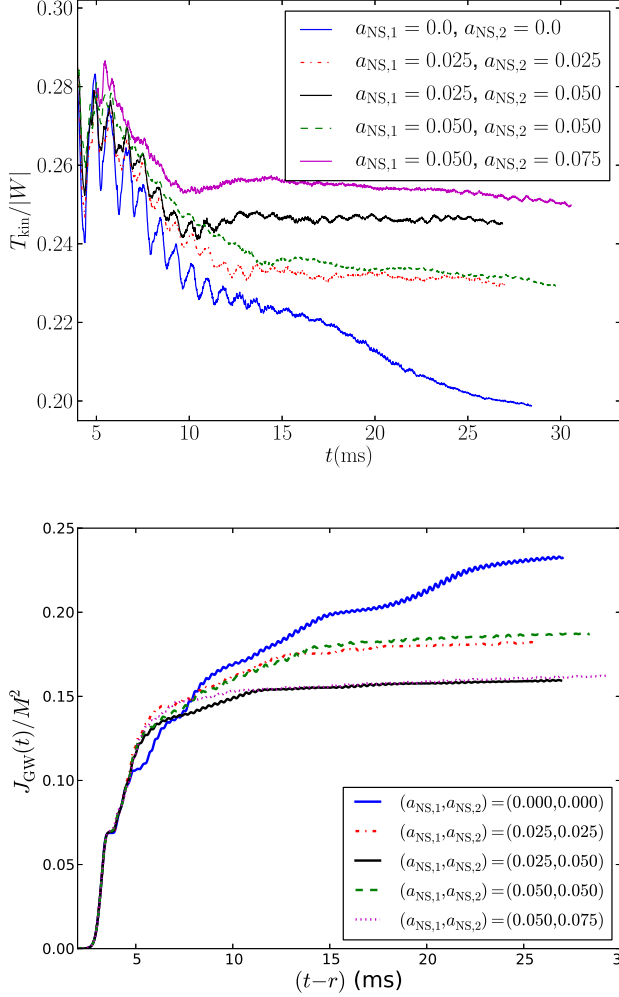


FIG. 16. Ratio of total kinetic to potential energy (top) and cumulative angular momentum emitted in GWs (bottom) for various low-spin $r_p/M = 8$ cases following merger. Data from high-resolution runs are plotted here.

tional instability (MRI). The former operates during the NSNS merger, while the latter operates following HMNS formation as long as the HMNS angular velocity is a decreasing function of the cylindrical radius measured from the HMNS rotation axis. Magnetic winding is another possibility, though since it leads to linear rather than exponential amplification on the rotational timescale [see Eq. (7) in [116]], it will be subdominant.

In [115] it was proposed that the turbulent eddies developing during merger can amplify the magnetic fields to magnetar-level strengths ($\sim 10^{16}$ G) in less than 1 ms. Recent global NSNS simulations, approaching the very high resolutions required to resolve this, indicate that this turbulent-dynamo mechanism indeed operates, though the magnetic field amplification seems to saturate on a longer timescale of ~ 5 ms following merger [117]

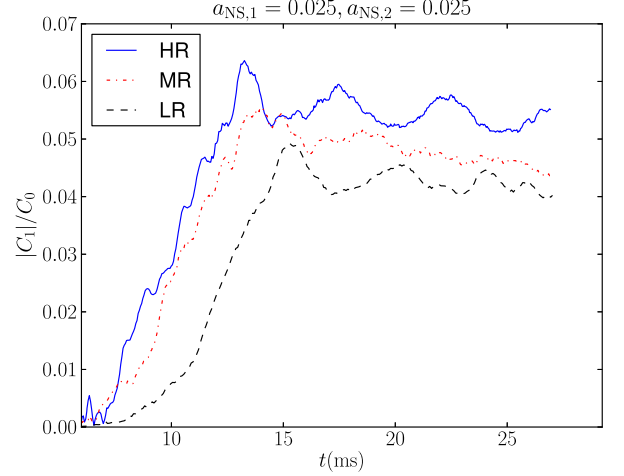


FIG. 17. Evolution of the amplitude in the $m = 1$ density mode for the high (HR), medium (MR), and low (LR) resolutions used in the $r_p/M = 8$, $a_{\text{NS},1} = a_{\text{NS},2} = 0.025$ case. We observe qualitative convergence of the growth time and early saturation amplitude with resolution.

and the rms value of the magnetic field strength at saturation is $\sim 10^{15.5}$ G.

For initially dynamically weak magnetic fields winding occurs on the local orbital period. Once the magnetic field tension becomes strong, winding occurs on the Alfvén timescale [118]. The left panel in Fig. 15 shows that prior to saturation of the $m = 1$ instability ($t < 13$ ms), when the velocity field is approximately axisymmetric (see right panel in Fig. 15), the angular velocity has a steep profile going from > 30000 rad/s near the center to ~ 8000 rad/s near the HMNS surface. This corresponds to orbital periods $P_{\text{orb}} < 0.2$ ms near the center to $P_{\text{orb}} \sim 0.8$ ms near the surface of the star. For a dynamically weak initial magnetic field, magnetic winding increases the strength of the toroidal magnetic field linearly with time [see Eq. (7) in [116]]

$$B \sim \Omega t (10^{10} \text{ G}), \quad (13)$$

where we have assumed an initial seed magnetic field of 10^{10} G and approximated derivatives by fractions. In our HMNSs the best case scenario for magnetic winding to build up the magnetic field fast is near the center where $P \sim 0.2$ ms. The time between HMNS formation and settling to saturation of the one-arm instability is ~ 10 ms, thus magnetic winding can amplify the initial magnetic field by at most $\sim 10/0.2 = 50$ times. In practice, the amplification factor will be $\mathcal{O}(10^2)$, because winding will start operating during merger. Thus, winding alone could amplify an initial magnetic field of 10^{10} G to $\sim 10^{12}$ G.

However, the magnetic field growth due to winding is completely subdominant compared to the growth due to MRI. The fact that for $t < 13$ ms, $\partial\Omega/\partial\varpi < 0$, renders

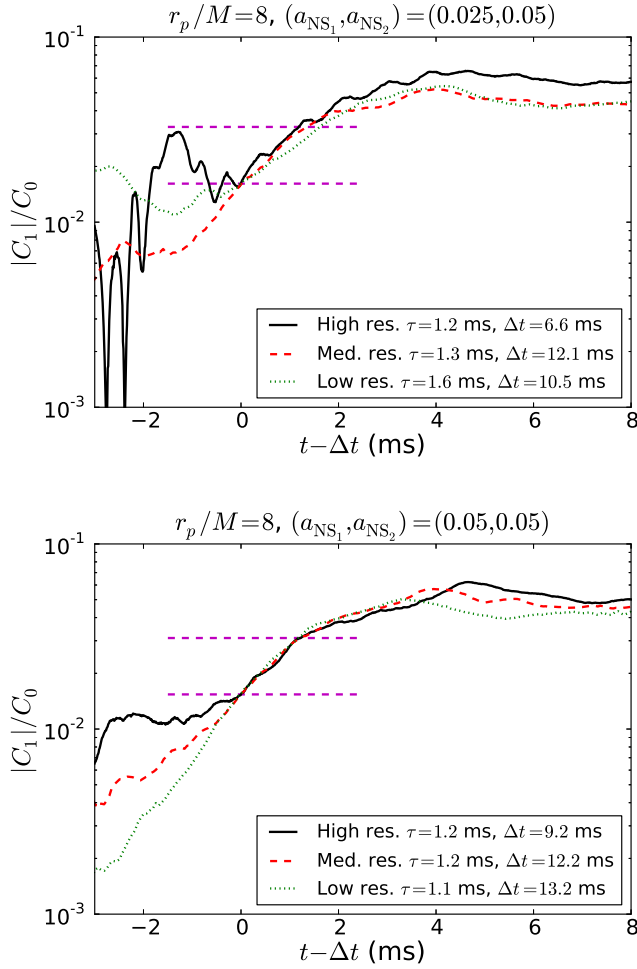


FIG. 18. Evolution of the amplitude in the $m = 1$ density mode for the high, medium, and low resolutions used in the $r_p/M = 8$, $(a_{\text{NS},1}, a_{\text{NS},2}) = (0.025, 0.05)$ (top) and $(0.05, 0.05)$ (bottom) cases. A time shift (indicated in the legend) is applied to each case so that curves are aligned at $t - \Delta t = 0$ with amplitude $1/4 \times$ the maximum amplitude of the highest resolution (indicated by the lower horizontal line). The growth rate τ (also indicated in the legend) measures the subsequent time required for amplitude to grow by a factor of two (upper horizontal line).

the HMNS unstable to the development of MRI, and unlike magnetic winding, which increases an initially dynamically weak magnetic field linearly with the orbital time, MRI increases the magnetic field exponentially on the same timescale. The e-folding time of the fastest growing MRI mode is [116]

$$t_{\text{MRI}} \sim \frac{1}{\Omega} \sim 0.1 \left(\frac{\Omega}{10^4 \text{ rad s}^{-1}} \right) \text{ ms}. \quad (14)$$

This implies that the initial seed magnetic field can be amplified through MRI from $\sim 10^{10}$ G to $\sim 10^{16}$ G in $\Delta t/t_{\text{MRI}} = 6 \ln(10) \sim 14$, or $\Delta t \sim 1.4$ ms. Thus, within

1.4 ms from the moment the HMNS becomes unstable to MRI, MRI can build up magnetar-level magnetic fields. Therefore, the HMNSs formed in our simulations can become strongly magnetized on a millisecond timescale even if the turbulent dynamo mechanism were not to operate as efficiently. The growth of the magnetic field due to MRI terminates when equipartition is reached. The results in the recent high-resolution NSNS simulations in [117] indicate that at saturation the magnetic energy is $\gtrsim 0.01 \times$ the bulk kinetic energy. This is consistent with what was found in [116] following saturation of the MRI in differentially rotating HMNSs. These results suggest that $B^2/8\pi \sim 0.5\rho_0 v^2/100$, which yields a characteristic magnetic field strength

$$B \sim 3 \times 10^{15} \left(\frac{\rho_0}{10^{15} \text{ gm/cm}^3} \right)^{1/2} \left(\frac{v}{0.1c} \right) \text{ G}, \quad (15)$$

where we used $v = 0.1c$ as the characteristic velocity shown in the right panel of Fig. 15. Note that the value of the magnetic field in Eq. (15) is consistent with the rms value found in [117].

However, although the magnetic fields should grow large on a $\mathcal{O}(1)$ ms timescale, if we assume, as above, that at saturation the growth of the magnetic field has not sapped the majority of the energy in differential rotation, the braking of the differential rotation will occur on an Alfvén timescale [116]

$$t_{\text{Alfvén}} \sim 40 \left(\frac{B}{3 \times 10^{15} \text{ G}} \right)^{-1} \left[\frac{(M_{\text{HMNS}}/R_{\text{HMNS}})}{0.3} \right]^{1/2} \text{ ms}. \quad (16)$$

Thus, the one-arm instability may have enough time to grow and develop following saturation of the magnetic fields, but the long-term survival will depend on the precise magnetic field strength at equipartition, and how magnetic fields interact with an $m = 1$ unstable mode. On the other hand, recent MHD simulations in full GR of magnetized, isolated relativistic stars [78] find that for low- $T/|W|$ isolated stars and dynamically weak initial seed magnetic fields $B < 10^{14}$ G, the magnetic field effects do not prevent shear instabilities from occurring, and conclude that the detection of GWs from such unstable modes is viable even when magnetic fields are accounted for. Thus, the one-arm instability found here may develop and thrive even in the presence of magnetic fields, but this must be investigated with further simulations that account for magnetic fields.

IV. CONCLUSIONS

In this work, we have performed simulations of dynamical capture NSNS mergers focusing on the effects of NS spin. We found that NS spin in NSNS mergers can have important consequences for the dynamics and outcome of these events. In the case that the NS spin is aligned with the orbital angular momentum, the additional angular momentum can lead to the formation

of a hypermassive NS compared to prompt BH formation with nonspinning (or lower spin) NSs. Conversely, when the NS spins are antialigned with the orbital angular momentum, the reduction in total angular momentum compared to the nonspinning case can cause prompt BH formation where otherwise a long lived hypermassive NS would have formed. We also demonstrate that even moderately high values of NS spin, corresponding to periods above a few ms, can significantly increase the total amount, and mean velocity, of unbound material ejected from the merger, which could lead to significantly brighter transients. For cases with significant NS spin we find examples with $\sim 0.1 M_\odot$ of ejected material, indicating that NS spin in NSNS mergers may be another way to explain putative kilonovae observations with very massive amounts of implied ejecta [119]. In contrast, simulations of quasicircular NSNS mergers with nonspinning NSs [30, 120] typically find ejecta masses $\lesssim 0.01 M_\odot$ – the upper limit reached only for soft EOS. In these simulations the average ejecta velocities found are $\sim 0.1\text{--}0.3c$, comparable to what we find here.

A remarkable feature discovered in our simulations of mergers involving NSNS binaries with total dimensionless angular momentum at merger of $J_{\text{ADM}}/M_{\text{ADM}}^2 \sim 0.9\text{--}1.0$ and not strong initial $m = 1$ azimuthal asymmetries is that the HMNSs that form post-merger develop the one-arm spiral instability [70]. We find growing $m = 1$ modes in cases involving higher spins as well, but the $m = 1$ remains subdominant to the $m = 2$ azimuthal density mode through the end of these simulations. The one-arm instability was first reported to occur in HMNSs arising in binary neutron star mergers in [69], and here we provided more details on the development of the instability and studied its dependence on the NS spin. We demonstrated that whenever the instability develops, it is manifested in the GWs from the post-merger phase, e.g., in a $l = 2, m = 1$ mode with similar GW frequency. This effect is potentially observable if there is a sufficiently large population of merger events where the instability persists and the HMNS can survive for on the order of seconds. Such long-lived HMNSs are believed to arise for sufficiently stiff EOSs [91], but it remains an open question as to whether the one-arm spiral instability can arise for stiff EOSs.

An interesting question that we cannot resolve here is why the instability was not observed in previous simulations. Perhaps it was present but the growth rate was insufficient in the particular scenarios modelled that a clear identification could not be made (e.g., growing $m = 1$ modes were reported in [63], but were described as possibly due to “mode couplings”; see also [27]). This circumstance would not be too surprising, as we found here that in some cases if the NSs are not spinning, the time from merger that it takes for the $m = 1$ density

mode to dominate over all other modes is about twice as long as when a small NS dimensionless spin of 0.025 is present, whereas most earlier studies of NSNS mergers focused on irrotational configurations. In other cases perhaps collapse to a BH took place before the instability had enough time to grow. On the other hand, it may be that only a limited range of eccentricities at merger, EOS, mass ratio and neutron star spins create conditions necessary for the instability to develop before collapse to a BH occurs. If the instability occurs only for a certain set of EOSs and range of masses, the accompanying $l = 2, m = 1$ mode of the GWs may prove a powerful probe of the nuclear EOS. Even if the $l = 2, m = 1$ mode of the GWs is present in all cases, correlations between the frequency of this mode and the EOS could also place constraints on the EOS. These are not questions we can address here, but will be topics of future work, as will the impact of magnetic fields and neutrino cooling on the development and saturation of the one-arm spiral instability.

Though we have focused on encounters that merge with sizable eccentricity, a portion of binary NSs that are dynamically assembled at large impact parameters will radiate away most of their orbital eccentricity well before merger. Thus, for GW detection, dense stellar environments could provide a population of quasicircular NSNS mergers that typically involve rapidly spinning NSs, and, moreover, where there is no preferential alignment of the spins relative to the orbital angular momentum. Since much of how spin affects the merger dynamics found here should carry over to that case, studying such systems would be interesting to investigate. Additionally, there is a larger parameter space including different orbital parameters, EOSs, spin orientations, etc. that need to be explored before a comprehensive understanding of binary NS mergers relevant to multi-messenger astronomy, including issues related to parameter degeneracies and estimation, is achieved.

ACKNOWLEDGMENTS

It is a pleasure to thank Andreas Bauswein, Roman Gold, and Jonathan Zrake for useful discussions. This work was supported by the Simons Foundation and NSF grant PHY-1305682 at Princeton University, as well as NSF grant PHY-1300903 and NASA grant NNX13AH44G at the University of Illinois at Urbana-Champaign. Computational resources were provided by XSEDE/TACC under grants TG-PHY100053, TG-MCA99S008, and the Orbital cluster at Princeton University.

[1] A. Abramovici et al., Science **256**, 325 (1992).

[2] B. Caron *et al.*, Class. Quant. Grav. **14**, 1461 (1997).

- [3] LCGT Collaboration, K. Somiya, *Class.Quant.Grav.* **29**, 124007 (2012), 1111.7185.
- [4] B. M. Hansen and M. Lyutikov, *Mon.Not.Roy.Astron.Soc.* **322**, 695 (2001), astro-ph/0003218.
- [5] S. T. McWilliams and J. Levin, *Astrophys. J.* **742**, 90 (2011), 1101.1969.
- [6] V. Paschalidis, Z. B. Etienne, and S. L. Shapiro, *Phys.Rev.* **D88**, 021504 (2013).
- [7] C. Palenzuela *et al.*, *Physical Review Letters* **111**, 061105 (2013), 1301.7074.
- [8] M. Ponce, C. Palenzuela, L. Lehner, and S. L. Liebling, *Phys. Rev.* **D90**, 044007 (2014), 1404.0692.
- [9] D. Tsang, J. S. Read, T. Hinderer, A. L. Piro, and R. Bondarescu, *Phys. Rev. Lett.* **108**, 011102 (2012).
- [10] D. Tsang, *Astrophys. J.* **777**, 103 (2013), 1307.3554.
- [11] B. D. Metzger and E. Berger, *Astrophys. J.* **746**, 48 (2012), 1108.6056.
- [12] E. Nakar and T. Piran, *Nature (London)* **478**, 82 (2011), 1102.1020.
- [13] K. Kyutoku, K. Ioka, and M. Shibata, *Mon. Not. Roy. Astron. Soc.* **437**, L6 (2014), 1209.5747.
- [14] B. D. Metzger, A. Bauswein, S. Goriely, and D. Kasen, *Mon. Not. Roy. Astron. Soc.* **446**, 1115 (2015), 1409.0544.
- [15] A. e. a. Rau, *PASP* **121**, 1334 (2009), 0906.5355.
- [16] N. Kaiser *et al.*, Pan-STARRS: A Large Synoptic Survey Telescope Array, in *Survey and Other Telescope Technologies and Discoveries*, edited by J. A. Tyson and S. Wolff, , Society of Photo-Optical Instrumentation Engineers (SPIE) Conference Series Vol. 4836, pp. 154–164, 2002.
- [17] LSST Dark Energy Science Collaboration, *ArXiv e-prints* (2012), 1211.0310.
- [18] T. Piran, *Reviews of Modern Physics* **76**, 1143 (2005).
- [19] P. Meszaros, *Rept.Prog.Phys.* **69**, 2259 (2006).
- [20] V. Paschalidis, M. Ruiz, and S. L. Shapiro, *Astrophys. J. Lett.* **806**, L14 (2015), 1410.7392.
- [21] S. Rosswog, F. K. Thielemann, M. B. Davies, W. Benz, and T. Piran, Coalescing Neutron Stars: a Solution to the R-Process Problem?, in *Nuclear Astrophysics*, edited by W. Hillebrandt and E. Muller, p. 103, 1998, arXiv:astro-ph/9804332.
- [22] J. A. Faber and F. A. Rasio, *ArXiv e-prints* (2012), 1204.3858.
- [23] T. W. Baumgarte and S. L. Shapiro, *Numerical Relativity: Solving Einstein's Equations on the Computer* (, 2010).
- [24] V. Paschalidis, Z. B. Etienne, and S. L. Shapiro, *Phys. Rev.* **D86**, 064032 (2012), 1208.5487.
- [25] D. Neilsen *et al.*, *Phys. Rev.* **D89**, 104029 (2014), 1403.3680.
- [26] B. Giacomazzo, J. Zrake, P. Duffell, A. I. MacFadyen, and R. Perna, *ArXiv e-prints* (2014), 1410.0013.
- [27] W. Kastaun and F. Galeazzi, *Phys. Rev.* **D91**, 064027 (2015), 1411.7975.
- [28] K. Dionysopoulou, D. Alic, and L. Rezzolla, *ArXiv e-prints* (2015), 1502.02021.
- [29] A. Bauswein and N. Stergioulas, *ArXiv e-prints* (2015), 1502.03176.
- [30] Y. Sekiguchi, K. Kiuchi, K. Kyutoku, and M. Shibata, *Phys. Rev.* **D91**, 064059 (2015), 1502.06660.
- [31] T. Dietrich, S. Bernuzzi, M. Ujevic, and B. Bruegmann, *ArXiv e-prints* (2015), 1504.01266.
- [32] C. Palenzuela *et al.*, *ArXiv e-prints* (2015), 1505.01607.
- [33] R. M. O'Leary, B. Kocsis, and A. Loeb, *Mon. Not. Roy. Astron. Soc.* **395**, 2127 (2009), 0807.2638.
- [34] B. Kocsis and J. Levin, *Phys. Rev.* **D85**, 123005 (2012), 1109.4170.
- [35] W. H. Lee, E. Ramirez-Ruiz, and G. van de Ven, *Astrophys. J.* **720**, 953 (2010), 0909.2884.
- [36] J. Samsing, M. MacLeod, and E. Ramirez-Ruiz, *Astrophys. J.* **784**, 71 (2014), 1308.2964.
- [37] C. L. Rodriguez *et al.*, *Phys. Rev. Lett.* **115**, 051101 (2015), 1505.00792.
- [38] W. E. East, S. T. McWilliams, J. Levin, and F. Pretorius, *Phys. Rev.* **D87**, 043004 (2013), 1212.0837.
- [39] R. Gold, S. Bernuzzi, M. Thierfelder, B. Brügmann, and F. Pretorius, *Phys. Rev.* **D86**, 121501 (2012), 1109.5128.
- [40] W. E. East and F. Pretorius, *Astrophys. J. Lett.* **760**, L4 (2012), 1208.5279.
- [41] B. Sathyaprakash *et al.*, *Classical and Quantum Gravity* **29**, 124013 (2012).
- [42] J. Grindlay, S. Portegies Zwart, and S. McMillan, *Nature Physics* **2**, 116 (2006), astro-ph/0512654.
- [43] R. Narayan, B. Paczynski, and T. Piran, *Astrophys. J.* **395**, L83 (1992), astro-ph/9204001, astro-ph/9204001.
- [44] N. G. *et al.*, *Nature (London)* **437**, 851 (2005), arXiv:astro-ph/0505630.
- [45] W. H. Lee, E. Ramirez-Ruiz, and J. Granot, *Astrophys. J. Lett.* **630**, L165 (2005), arXiv:astro-ph/0506104.
- [46] T. A. Thompson, *Astrophys. J.* **741**, 82 (2011), 1011.4322.
- [47] B. Katz, S. Dong, and R. Malhotra, *Physical Review Letters* **107**, 181101 (2011), 1106.3340.
- [48] N. Seto, *Physical Review Letters* **111**, 061106 (2013), 1304.5151.
- [49] F. Antonini *et al.*, *ArXiv e-prints* (2015), 1509.05080.
- [50] B. C. Stephens, W. E. East, and F. Pretorius, *Astrophys. J. Lett.* **737**, L5 (2011), 1105.3175.
- [51] W. E. East, F. Pretorius, and B. C. Stephens, *Phys. Rev. D* **85**, 124009 (2012).
- [52] W. H. Lee, E. Ramirez-Ruiz, and G. van de Ven, *Astrophys. J.* **720**, 953 (2010), 0909.2884.
- [53] S. Rosswog, T. Piran, and E. Nakar, *Mon. Not. Roy. Astron. Soc.* **430**, 2585 (2013), 1204.6240.
- [54] W. E. East, V. Paschalidis, and F. Pretorius, *Astrophys. J. Lett.* **807**, L3 (2015), 1503.07171.
- [55] www.naic.edu/~pfreire/GCpsr.html.
- [56] F. Verbunt and P. Hut, The Globular Cluster Population of X-Ray Binaries, in *The Origin and Evolution of Neutron Stars*, edited by D. J. Helfand and J.-H. Huang, , IAU Symposium Vol. 125, p. 187, 1987.
- [57] F. Lamb and W. Yu, Spin Rates and Magnetic Fields of Millisecond Pulsars, in *Binary Radio Pulsars*, edited by F. A. Rasio and I. H. Stairs, , Astronomical Society of the Pacific Conference Series Vol. 328, p. 299, 2005, astro-ph/0408459.
- [58] P. Ghosh and F. K. Lamb, *Astrophys. J.* **234**, 296 (1979).
- [59] T. M. Tauris, N. Langer, and M. Kramer, *Mon. Not. Roy. Astron. Soc.* **425**, 1601 (2012), 1206.1862.
- [60] B. A. Jacoby *et al.*, *Astrophys. J. Lett.* **644**, L113 (2006), astro-ph/0605375.
- [61] R. S. Lynch, P. C. C. Freire, S. M. Ransom, and B. A. Jacoby, *Astrophys. J.* **745**, 109 (2012), 1112.2612.
- [62] W. Tichy, *Phys.Rev.* **D84**, 024041 (2011), 1107.1440.

- [63] S. Bernuzzi, T. Dietrich, W. Tichy, and B. Bruegmann, *Phys.Rev.* **D89**, 104021 (2014), 1311.4443.
- [64] T. Dietrich *et al.*, ArXiv e-prints (2015), 1507.07100.
- [65] N. Tacik *et al.*, ArXiv e-prints (2015), 1508.06986.
- [66] P. Tsatsin and P. Marronetti, *Phys. Rev.* **D88**, 064060 (2013), 1303.6692.
- [67] W. Kastaun, F. Galeazzi, D. Alic, L. Rezzolla, and J. A. Font, *Phys. Rev.* **D88**, 021501 (2013), 1301.7348.
- [68] A. Bauswein, N. Stergioulas, and H.-T. Janka, ArXiv e-prints (2015), 1508.05493.
- [69] V. Paschalidis, W. E. East, F. Pretorius, and S. L. Shapiro, ArXiv e-prints (2015), 1510.03432.
- [70] J. M. Centrella, K. C. B. New, L. L. Lowe, and J. D. Brown, *Astrophys. J. Lett.* **550**, L193 (2001), astro-ph/0010574.
- [71] M. Saijo, T. W. Baumgarte, and S. L. Shapiro, *Astrophys. J.* **595**, 352 (2003), astro-ph/0302436.
- [72] A. L. Watts, N. Andersson, and D. I. Jones, *Astrophys. J. Lett.* **618**, L37 (2005), astro-ph/0309554.
- [73] M. Saijo and S. Yoshida, *Mon. Not. Roy. Astron. Soc.* **368**, 1429 (2006), astro-ph/0505543.
- [74] M. Shibata, S. Karino, and Y. Eriguchi, *Mon. Not. Roy. Astron. Soc.* **334**, L27 (2002), gr-qc/0206002.
- [75] M. Shibata, S. Karino, and Y. Eriguchi, *Mon. Not. Roy. Astron. Soc.* **343**, 619 (2003), astro-ph/0304298.
- [76] S. Ou and J. E. Tohline, *Astrophys. J.* **651**, 1068 (2006), astro-ph/0604099.
- [77] G. Corvino, L. Rezzolla, S. Bernuzzi, R. De Pietri, and B. Giacomazzo, *Classical and Quantum Gravity* **27**, 114104 (2010), 1001.5281.
- [78] C. D. Muhlberger *et al.*, *Phys. Rev.* **D90**, 104014 (2014), 1405.2144.
- [79] C. D. Ott, S. Ou, J. E. Tohline, and A. Burrows, *Astrophys. J. Lett.* **625**, L119 (2005), astro-ph/0503187.
- [80] C. D. Ott *et al.*, *Physical Review Letters* **98**, 261101 (2007), astro-ph/0609819.
- [81] T. Kuroda, T. Takiwaki, and K. Kotake, *Phys. Rev.* **D89**, 044011 (2014), 1304.4372.
- [82] W. E. East, F. Pretorius, and B. C. Stephens, *Phys. Rev. D* **85**, 124010 (2012).
- [83] W. E. East, F. M. Ramazanoglu, and F. Pretorius, *Phys.Rev.* **D86**, 104053 (2012), 1208.3473.
- [84] G. B. Cook, S. L. Shapiro, and S. A. Teukolsky, *Astrophys. J.* **424**, 823 (1994).
- [85] G. B. Cook, S. L. Shapiro, and S. A. Teukolsky, *Astrophys. J.* **422**, 227 (1994).
- [86] J. S. Read *et al.*, *Phys. Rev.* **D79**, 124033 (2009), 0901.3258.
- [87] I. A. Morrison, T. W. Baumgarte, and S. L. Shapiro, *Astrophys. J.* **610**, 941 (2004), astro-ph/0401581.
- [88] M. Shibata, T. W. Baumgarte, and S. L. Shapiro, *Astrophys. J.* **542**, 453 (2000), astro-ph/0005378.
- [89] N. Stergioulas, *Living Reviews in Relativity* **3** (2003).
- [90] K. Kiuchi, M. Shibata, and S. Yoshida, *Phys. Rev.* **D78**, 024029 (2008), 0805.2712.
- [91] Y. Sekiguchi, K. Kiuchi, K. Kyutoku, and M. Shibata, *Phys. Rev. Lett.* **107**, 051102 (2011).
- [92] K. Taniguchi and E. Gourgoulhon, *Phys. Rev.* **D68**, 124025 (2003), arXiv:gr-qc/0309045.
- [93] M. Turner, *Astrophys. J.* **216**, 610 (1977).
- [94] D. Shoemaker, Advanced LIGO Anticipated Sensitivity Curves, 2011, <https://dcc.ligo.org/cgi-bin/DocDB/ShowDocument?docid=2974>.
- [95] S. Hild *et al.*, *Classical and Quantum Gravity* **28**, 094013 (2011), 1012.0908.
- [96] M. Shibata and K. Taniguchi, *Phys. Rev.* **D73**, 064027 (2006), arXiv:astro-ph/0603145.
- [97] L. Baiotti, B. Giacomazzo, and L. Rezzolla, *Phys. Rev.* **D78**, 084033 (2008), 0804.0594.
- [98] K. Kiuchi, K. Kyutoku, Y. Sekiguchi, M. Shibata, and T. Wada, *Phys. Rev.* **D90**, 041502 (2014), 1407.2660.
- [99] L.-X. Li and B. Paczynski, *Astrophys.J.* **507**, L59 (1998), astro-ph/9807272.
- [100] S. R. Kulkarni, ArXiv Astrophysics e-prints (2005), arXiv:astro-ph/0510256.
- [101] B. D. Metzger *et al.*, *Mon. Not. Roy. Astron. Soc.* **406**, 2650 (2010), 1001.5029.
- [102] J. Barnes and D. Kasen, *Astrophys. J.* **775**, 18 (2013), 1303.5787.
- [103] D. Kasen, N. R. Badnell, and J. Barnes, *Astrophys. J.* **774**, 25 (2013), 1303.5788.
- [104] J. M. Lattimer and D. N. Schramm, *Astrophys. J. Lett.* **192**, L145 (1974).
- [105] T. Fischer, S. C. Whitehouse, A. Mezzacappa, F.-K. Thielemann, and M. Liebendörfer, *A&A* **517**, A80 (2010).
- [106] A. Arcones and H.-T. Janka, *A&A* **526**, A160 (2011).
- [107] A. Wallner *et al.*, *Nature Communications* **6**, 5956 (2015).
- [108] E. Ramirez-Ruiz *et al.*, *Astrophys. J. Lett.* **802**, L22 (2015), 1410.3467.
- [109] Y.-Z. Qian, *Astrophys. J. Lett.* **534**, L67 (2000), astro-ph/0003242.
- [110] J. Abadie *et al.*, *Classical and Quantum Gravity* **27**, 173001 (2010), 1003.2480.
- [111] N. Stergioulas, A. Bauswein, K. Zagkouris, and H.-T. Janka, (2011), 1105.0368.
- [112] K. Takami, L. Rezzolla, and L. Baiotti, *Physical Review Letters* **113**, 091104 (2014), 1403.5672.
- [113] K. Takami, L. Rezzolla, and L. Baiotti, *Phys. Rev.* **D91**, 064001 (2015), 1412.3240.
- [114] A. Bauswein, N. Stergioulas, and H.-T. Janka, ArXiv e-prints (2015), 1503.08769.
- [115] J. Zrake and A. I. MacFadyen, *Astrophys. J. Lett.* **769**, L29 (2013), 1303.1450.
- [116] M. D. Duez, Y. T. Liu, S. L. Shapiro, M. Shibata, and B. C. Stephens, *Phys. Rev.* **D73**, 104015 (2006), arXiv:astro-ph/0605331.
- [117] K. Kiuchi, P. Cerda-Duran, K. Kyutoku, Y. Sekiguchi, and M. Shibata, (2015), 1509.09205.
- [118] S. L. Shapiro, *Astrophys. J.* **544**, 397 (2000), astro-ph/0010493.
- [119] B. Yang *et al.*, *Nature Communications* **6**, 7323 (2015), 1503.07761.
- [120] C. Palenzuela *et al.*, ArXiv e-prints (2015), 1505.01607.